International Journal of Solids and Structures 202 (2020) 532–551

Contents lists available at ScienceDirect

International Journal of Solids and Structures

journal homepage: www.elsevier.com/locate/ijsolstr

Propagating material instabilities in planar architectured materials

Antoine-Emmanuel Viard [a,b], Justin Dirrenberger [a,*], Samuel Forest [b]

[a] Laboratoire PIMM, Arts et Métiers, CNRS, Cnam, Paris, France
[b] MINES ParisTech, PSL University, Centre des matériaux (CMAT), CNRS UMR 7633, 91003 Evry, France

ARTICLE INFO

Article history:
Received 23 October 2019
Received in revised form 13 February 2020
Accepted 20 May 2020
Available online 8 July 2020

Keywords:
Piobert-Lüders instabilities
Architectured materials
Computational mechanics
Experimental testing
Finite element analysis
Elastoplasticity

ABSTRACT

Under tension low carbon steel exhibits inhomogeneous plastic deformation. This instability called Piobert-Lüders banding creates fronts of localized strain that propagate in the structure. To date, Lüders banding has been studied experimentally and numerically only in simple geometries like sheets, tubes and normalized fracture mechanics specimens. This paper focuses on architectured materials and specifically lattice structures which can be defined as a tessellation of unit-cells periodically distributed in space. This class of advanced materials draws new mechanical properties from its inner architecture.

We investigate the effect of the architecture on the global behavior of the structure. Especially, how bands interact with the lattice and how to control initiation and propagation of localized strain using the architecture. An elastoplastic material model is used in order to simulate the Piobert-Lüders band formation and propagation. The model also considers a large deformation framework for elastoplasticity with periodic boundary conditions in order to represent the architectured material. Initiation and propagation of material instabilities depend on the geometry as well as its on the relative orientation with respect to the loading direction. Propagating and non-propagating behaviors are identified for the Piobert-Lüders bands and related to the different types of geometry. Material instabilities affect the mechanical behavior of the structure as far as they are governed by the architecture. These conclusions are compared to experimental results from tensile tests on laser-architectured specimens made of ARMCO steel.

1. Introduction

Architectured materials, in the sense given by Ashby and Bréchet (2003), Bouaziz et al. (2008), Bréchet (2013), Bréchet and Embury (2013) and Ashby (2013), are obtained from a design process aiming at fulfilling a specific set of requirements through a given functionality, behavior, or performance, induced via a particular morphological arrangement between multiple material phases. Among architectured materials, lattices are a specific kind of cellular materials, *i.e.* a combination of material and space. Lattice structures are composed of a connected network of struts, that may be organized periodically in space. They are generally used in cases where there is a need for either high specific stiffness, or high specific strength, but are also the basis of mechanical metamaterials (Ashby, 2006; C eté et al., 2006; Zok et al., 2016; Nassar et al., 2016; Combescure and Elliott, 2017; Poncelet et al., 2018; Rosi et al., 2018; Latture et al., 2018; Turco et al., 2018; dell'Isola et al., 2018; Onal et al., 2018; Rosi and Auffray, 2019). Modeling the mechanical response of architectured materials, especially lattice structures, is of prime interest for enabling their use in industrial applications. From an analytical viewpoint, models have been available for the description of the elastic behavior of cellular and lattice materials based on a strength of materials approach. Beyond the classical elastic behavior of cellular materials, (Gibson and Ashby, 1999) proposed a description based on geometrical and material parameters for the nonlinear behavior of lattices, *e.g.* plastic buckling, toughness. Following the seminal work by Gibson and Ashby, 2D topologies were widely studied using both analytical and numerical models (Wang and McDowell, 2004; Wang and McDowell, 2005; Fleck and Qiu, 2007; Alonso and Fleck, 2007) in order to improve the description of elastoplasticity and failure of such materials. By taking into account the deflection of inclined struts in lattices, *i.e.* extending the analytical model to large deformations, (Guoming et al., 2006) improved the description of elastic moduli in 2D cellular materials given in Gibson and Ashby (1999).

In the same way, (Tankasala et al., 2017) investigated the tensile response of lattices at finite strains. A description of various regimes from buckling to fracture in lattices under tension was given. Using an elastic perfectly-plastic material model, (Bonfanti et al., 2016; Bonfanti and Bhaskar, 2018) focused on the nonlinear plastic response of cell walls in 2D lattices under combined loads. A

* Corresponding author.

https://doi.org/10.1016/j.ijsolstr.2020.05.027
0020-7683/

study of geometrical instabilities trough computational modeling completed by experimental testing in 2D cellular materials is proposed by Niknam and Akbarzadeh (2018).

Most of the previous studies generally consider perfect elasto-plastic models to study plasticity in lattices. Another type of instabilities is related to the microstructure for some materials, *e.g.* mild steel, aluminum alloy, etc. This is the so-called Piobert-Lüders (Piobert, 1842; Lüders, 1860) phenomenon, which occurs during the initiation of plasticity and causes localized plastic deformation as bands that propagate along the specimen. The question arises of the interaction of such static strain ageing instabilities with the architecture of the lattice. To the knowledge of the authors, this problem has never addressed for lattice structures. For example, Kyriakides et al. (2008) studied, numerically and experimentally, the interaction between Lüders banding and buckling of steel bars. Another example in which the architecture can alter the modes of buckling of a structure has been presented by He et al. (2018) exploring different geometry for vertices in a square lattice. Hallai and Kyriakides (2011) emphasized the role of the propagation of Piobert-Lüders bands in the emergence of a propagating non-uniform curvature during the bending of steel tubes.

The localized nature of the Piobert-Lüders bands can lead to premature collapse if not properly accounted in the design. On the other hand, one could take advantage of these instabilities for instance by controlling them through the architecture.

In this article, we are interested in the interaction between the Piobert-Lüders phenomenon and 2D-lattices with different topologies covering both bending- and stretch-dominated behaviors. The objective of the present paper is to simulate the initiation and propagation of Piobert-Lüders bands within planar architectured media and to study how such material instabilities affect the mechanical response of architectured materials. This work aims at a classification of architectures enabling or impeding the propagation of localized deformation modes induced by the Piobert–Lüders bands occuring in the struts.

This paper is organized as follows: firstly, finite deformation elastoplastic model accounting for Piobert-Lüders is presented. In the same section, three archetypal geometries are introduced for the subsequent simulations and experiments. The initial boundary value problem including periodic boundary conditions is formulated and finite element simulation results are reported in Section 3. The macroscopic behavior of each lattice is analyzed in the light of accumulated plastic strain maps. Section 4 deals with the issue of the proper volume element size to be considered in the presence of instabilities while considering periodic boundary conditions. An experimental validation of the predicted instability propagation properties is proposed in Section 5 for the considered architectured. For that purpose finite size samples with a limited number of cells are tested to investigate the localization phenomena at the local and global scales. The experimental results are compared to finite element simulations on the whole samples. A thorough discussion of the results is presented in Section 6 and concluding remarks are provided in Section 7.

The following notations are used throughout: first, second and fourth order tensors are respectively denoted by $\underline{\boldsymbol{a}}$, $\underset{\sim}{\boldsymbol{b}}$ and $\underset{\approx}{\boldsymbol{C}}$. The double contraction is written $\underset{\sim}{\boldsymbol{a}} : \underset{\sim}{\boldsymbol{a}} = a_{ij}a_{ij}$.

2. Periodic media and material instabilities

2.1. Lattice structure

A lattice structure can be defined as a tessellation of unit-cells periodically distributed in space. In the following, we are only interested in 2D lattices. Numerous studies focused on the behavior of these architectures and they are classically divided into two different groups depending on their main deformation mode: (i) bending-dominated or (ii) stretch-dominated, as shown in Fig. 1.

(i) Bending-dominated: as in Fig. 1, the first configuration (a) is a mechanism according to Deshpande et al. (2001). When loaded, it can deform thanks to the rotation of pin-joints and induces bending in the struts caused by rigidity of the joints. It exhibits low stiffness and low strength.
(ii) Stretch-dominated: as in Fig. 1, the second configuration (b) is a structure as explained in the work of Deshpande et al. (2001). When loaded, struts are either in tension or in compression thanks to the higher connectivity between joints. Joints are mostly not rotating and the deformation is stretch-dominated. Such structures usually exhibit higher stiffness and strength than bending-dominated lattices.

This study focuses on the in-plane finite strain tensile response of three representative topologies: triangular, square and hexagonal as shown in Fig. 2. These ideal structures display a large variety of mechanical responses, which justifies the choice of those topologies.

The triangular and the hexagonal lattices are invariant by a 60° rotation, the square by a 90°. As explained in Auffray et al. (2015) and Tankasala et al. (2017), the triangular and the hexagonal lattices are isotropic in-plane for linear elasticity, but anisotropic for non-linear behavior. The triangular lattice is stiff and belongs to the stretch-dominated structures while the hexagonal lattice is bending-dominated and exhibits a more compliant behavior. On the contrary, the square lattice exhibits quadratic anisotropy in-plane for linear elasticity. It displays a stretch-dominated behavior if loaded along its struts and a bending-dominated behavior when struts are oriented by 45° with respect to the loading direction. Therefore, it is interesting to study which direction and which geometry promote the propagation of plastic strain bands. The three architectures will be loaded in all possible in-plane directions taking into account their symmetry. Each unit cell is defined by the length and thickness of its struts. For each lattice, the relative density is fixed to 30% and the length to 1. The corresponding thickness of the struts of each lattice reported in Table 1 for each geometry.

2.2. Phenomenological modeling of the Piobert-Lüders phenomenon

The Piobert-Lüders instability in low carbon steel characterizes the transition from the elastic to the plastic deformation regimes corresponding to the release of dislocations pinned by interstitial atoms. Macroscopically, it generally results in the emergence and subsequent propagation of plastic deformation bands.

An elastoplastic material model is used in this work in order to simulate the Piobert-Lüders band formation and propagation. The model accounts for large deformations as needed because of the high strain levels experienced locally by the different geometries studied in Section 3.

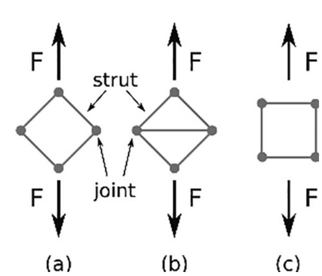

Fig. 1. (a) a mechanism; (b) a structure; (c) self-stressed state mechanism adapted from Deshpande et al. (2001).

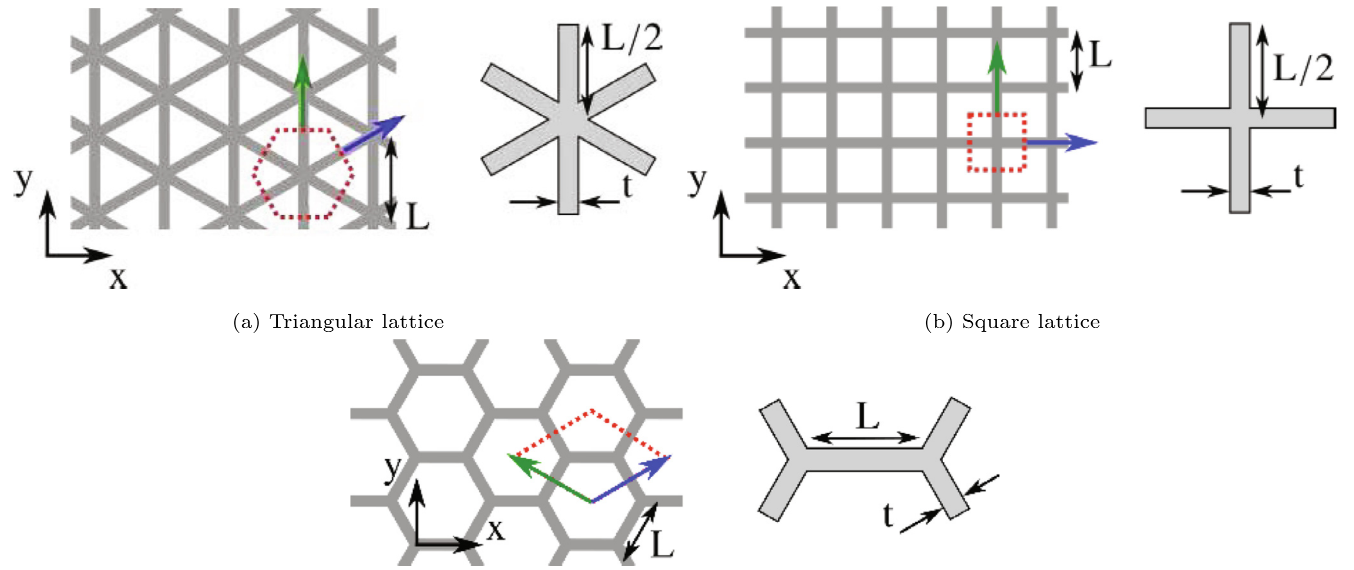

(a) Triangular lattice

(b) Square lattice

(c) Hexagonal lattice

Fig. 2. Lattice topologies and their corresponding unit cells employed for the FE simulation with their periodic vectors. (a) triangular lattice, (b) square lattice and (c) hexagonal lattice.

Table 1
Thickness of struts for a 30% relative density and a length of 1.

	Triangle	Diamond	Hexagon
Thickness	0.09	0.15	0.26

The finite deformation formulation chosen in the present work for isotropic nonlinear material behavior is based on a co-rotational transformation of the stress rate-strain rate problem making use of a local objective frame. This framework developed in Ladevèze (1980), Dogui and Sidoroff (1986) and Besson et al. (2009) allows for the extension of constitutive laws from infinitesimal strain to large deformation without modification of the form of the plastic flow and hardening rules. $\underset{\sim}{\dot{\boldsymbol{e}}}$ and $\underset{\sim}{\boldsymbol{s}}$ are the invariant strain rate and stress measures defined by transport of the Eulerian strain rate $\underset{\sim}{\boldsymbol{D}}$ and the Cauchy stress $\underset{\sim}{\boldsymbol{T}}$ into the local objective frame $\mathbf{E}'$. The evolution from $\mathbf{E}$ to $\mathbf{E}'$ is characterized by the rotation $\underset{\sim}{\mathbf{Q}}(\underset{\sim}{\boldsymbol{x}}, t)$. The velocity gradient $\underset{\sim}{\boldsymbol{L}}$ defined as $\underset{\sim}{\boldsymbol{L}} = \underset{\sim}{\dot{\boldsymbol{F}}}.\underset{\sim}{\boldsymbol{F}}^{-1}$ where $\underset{\sim}{\boldsymbol{F}}$ is the usual deformation gradient. $\underset{\sim}{\boldsymbol{L}}$ is decomposed into its symmetric and skew parts, $\underset{\sim}{\boldsymbol{D}}$ and $\underset{\sim}{\boldsymbol{\Omega}}$.

$$\begin{cases} \underset{\sim}{\dot{\boldsymbol{e}}} = \underset{\sim}{\mathbf{Q}}^{\mathrm{T}} . \underset{\sim}{\boldsymbol{D}} . \underset{\sim}{\mathbf{Q}} \\ \underset{\sim}{\boldsymbol{s}} = \underset{\sim}{\mathbf{Q}}^{\mathrm{T}} . \underset{\sim}{\boldsymbol{T}} . \underset{\sim}{\mathbf{Q}} \\ \underset{\sim}{\mathbf{Q}} \text{ such that } \underset{\sim}{\dot{\mathbf{Q}}}^{\mathrm{T}} . \underset{\sim}{\mathbf{Q}} = \underset{\sim}{\boldsymbol{\Omega}} \end{cases} \tag{1}$$

The strain rate tensor $\underset{\sim}{\dot{\boldsymbol{e}}}$ is split into elastic and plastic parts. The yield function is $f(\underset{\sim}{\boldsymbol{s}}, R)$. The rate-independent elastoplasticity model for large deformation is finally written as:

$$\begin{cases} \underset{\sim}{\dot{\boldsymbol{e}}} = \underset{\sim}{\dot{\boldsymbol{e}}}^{e} + \underset{\sim}{\dot{\boldsymbol{e}}}^{p} \\ f(\underset{\sim}{\boldsymbol{s}}, R) = J_2(\underset{\sim}{\boldsymbol{s}}) - R(p) \\ \underset{\sim}{\dot{\boldsymbol{e}}}^{p} = \dot{p}\frac{\partial f}{\partial \underset{\sim}{\boldsymbol{s}}}, \; \dot{p} \geqslant 0 \\ \underset{\sim}{\boldsymbol{s}} = \underset{\approx}{\boldsymbol{C}} : \underset{\sim}{\dot{\boldsymbol{e}}}^{e} \end{cases} \tag{2}$$

where $R(p)$ is the yield stress taken as a function of the accumulated plastic strain p.

A von Mises criterion is chosen for f with $J_2(\underset{\sim}{\boldsymbol{s}}) = \sqrt{\frac{3}{2}\underset{\sim}{\boldsymbol{s}}^{\mathrm{dev}} : \underset{\sim}{\boldsymbol{s}}^{\mathrm{dev}}}$, the second invariant of the stress tensor and $\underset{\sim}{\boldsymbol{s}}^{\mathrm{dev}}$ is the deviatoric part of the stress tensor.

2.3. Numerical approach of the Piobert-Lüders phenomenon

Tsukahara and Iung (1998) introduced a local behavior modeling the Piobert-Lüders behavior by the finite element method. It consists in a description of the work-hardening material function as linear softening branch followed by a linear hardening branch. Later, Ballarin et al. (2009) smoothened this behavior hardening potentials evolving non linearly with p.

$$R(p) = R_0 + Q_1(1 - e^{-b_1 p}) + Q_2(1 - e^{-b_2 p}) + Q_3(1 - e^{-b_3 p}) \tag{3}$$

The elastic behavior is described by the Young modulus and the Poisson ratio, equal to 210 GPa and 0.3, respectively. Regarding the plastic behavior, a softening term $(Q_2;b_2)$ added to a Voce strain hardening law described by the initial yield stress R_0 and the parameters $(Q_1;b_1)$ with $Q_1 > 0$ and $Q_2 < 0$. Static strain aging is modeled by the negative potential Q_2. The third function $(Q_3;b_3)$ is added to the initial model to smooth out the peak stress for better convergence during finite element simulation (Marais et al., 2012). The corresponding values of the parameters are given in Table 2. These parameters are chosen to replicate a 2% strain long stress plateau at 90 MPa and a stress peak at 100 MPa as shown in Fig. 3. On the same figure, the softening branch of the function $R(p)$ is visible in the constitutive response of a material point. It is well-known that such a softening branch is unstable and leads to the formation of a localization band right after the peak stress (Mazière and Forest, 2015). This is illustrated by the finite element simulation of a plate in tension with the corresponding overall stress (force divided by the initial section) and applied overall strain curve in Fig. 3. 3D computation has been performed in order to minimize constraint on the behavior of instabilities. The formation and propagation of Piobert-Lüders band in such a plate in tension is illustrated in Fig. 4. This phenomenological approach is used

Table 2
Parameters for the phenomenological plasticity model.

R_0 (MPa)	Q_1 (MPa)	b_1	Q_2 (MPa)	b_2	Q_3 (MPa)	b_3
100	400	10	−100	80	5	300

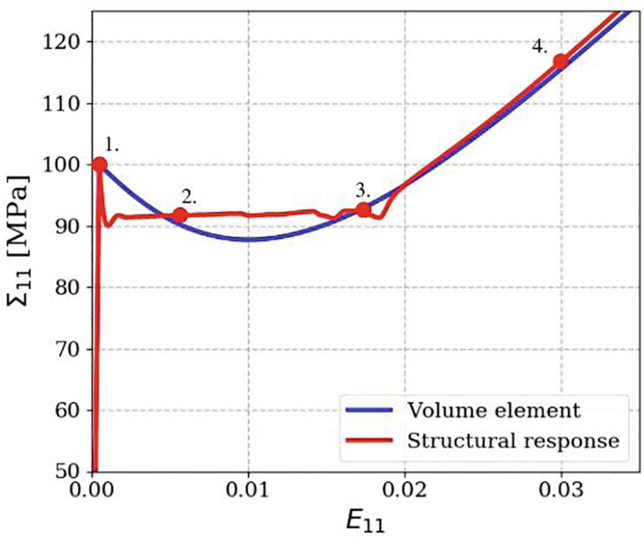

Fig. 3. Intrinsic consitutive law for Piobert-Lüders phenomenon integrated on a single Gauss point (Volume element) compared to the overall response of a plate endowed with this material behavior. The accumulated plastic strain maps corresponding to the points (1,2,3,4) marked on the plate response curve are shown in Fig. 4.

to mimic the Piobert-Lüders effect in our simulations. Macroscopically, it yields a stress plateau at a lower value than the peak, as shown in Fig. 3. After the propagation of the band throughout the specimen, homogeneous hardening starts taking place.

3. Propagation of material instabilities in infinite periodic media

3.1. Periodic boundary value problem

Investigated lattices are periodic in plane. The homogenized behavior of the structure is found from the unit-cell with appropriate periodic boundary conditions. The reference configuration of the unit cell is called V_0 whereas the current state at time t is V. The displacement field and the Cauchy stress tensor inside the unit cell are respectively called $\underline{\boldsymbol{u}}$ and $\underset{\sim}{\boldsymbol{\sigma}}$. The macroscopic strain and Cauchy stress tensors are defined as spatial averages over the unit cell:

$$
\begin{aligned}
\underset{\sim}{\boldsymbol{E}} &= \frac{1}{V_0}\int_{V_0} \mathrm{Grad}\,\underline{\boldsymbol{u}}\,dV_0 \\
\underset{\sim}{\boldsymbol{\Sigma}} &= \frac{1}{V}\int_{V} \underset{\sim}{\boldsymbol{\sigma}}\,dV
\end{aligned}
\tag{4}
$$

The gradient operator Grad is computed with respect to Lagrange coordinates. Note that the conjugate of $\underset{\sim}{\boldsymbol{E}}$ in the work of internal forces is the Boussinesq tensor, also called first Piola–Kirchhoff stress tensor. However we will use the effective Cauchy stress $\underset{\sim}{\boldsymbol{\Sigma}}$ for post-processing the results of the finite element simulations.

The periodic boundary value problem over the unit cell aims at finding the local displacement field $\underline{\boldsymbol{u}}$ as the sum of a macroscopic part and a periodic fluctuation:

$$
\underline{\boldsymbol{u}} = \underset{\sim}{\boldsymbol{E}}\cdot\underline{\boldsymbol{X}} + \underline{\boldsymbol{v}} \tag{5}
$$

where $\underset{\sim}{\boldsymbol{E}}$ is the prescribed macroscopic strain tensor and $\underline{\boldsymbol{X}}$ denote the Lagrange reference coordinates. Applying the macroscopic strain $\underset{\sim}{\boldsymbol{E}}$, one computes the fluctuation vector on the unit cell. The uniform strain distribution $\underset{\sim}{\boldsymbol{E}}$ would be the strain of the medium if it were homogeneous and $\underline{\boldsymbol{v}}$ represents an in-plane periodic fluctuation of the displacement due to local inhomogeneities of the material and in this present case to the architecture. Thus, the strain and stress fields over the infinite structure vary in a periodic manner around the mean values $\underset{\sim}{\boldsymbol{E}}$ and $\underset{\sim}{\boldsymbol{\Sigma}}$ with a periodicity equal to the unit cell size. The periodic boundary conditions mean that the fluctuation $\underline{\boldsymbol{v}}$ takes the same value at homologous points on opposite sides of the cell, such that:

$$
\forall(\underline{\boldsymbol{x}}^-;\underline{\boldsymbol{x}}^+)\in(\partial\Omega^-;,\partial\Omega^+),\ \underline{\boldsymbol{v}}(\underline{\boldsymbol{x}}^-) = \underline{\boldsymbol{v}}(\underline{\boldsymbol{x}}^+) \tag{6}
$$

whereas the traction vector $\underset{\sim}{\boldsymbol{\sigma}}\cdot\underline{\boldsymbol{n}}$ is anti-periodic:

$$
\forall(\underline{\boldsymbol{x}}^-;\underline{\boldsymbol{x}}^+)\in(\partial\Omega^-;,\partial\Omega^+),\ \underset{\sim}{\boldsymbol{\sigma}}(\underline{\boldsymbol{x}}^-).\underline{\boldsymbol{n}}(\underline{\boldsymbol{x}}^-) = -\underset{\sim}{\boldsymbol{\sigma}}(\underline{\boldsymbol{x}}^+).\underline{\boldsymbol{n}}(\underline{\boldsymbol{x}}^+) \tag{7}
$$

Our computational homogenization calculations will rely on the periodic finite element available in the Z-Set finite element package, making it possible to prescribe mixed boundary conditions like in the tensile tests considered in the following. For that purpose, the macroscopic strain E_{11} is prescribed and all the macroscopic stress components Σ_{ij} are fixed to zero, except Σ_{11}.

A Newton algorithm is used to solve the global equilibrium equations based on the finite element method with a total Lagrangian formulation. An implicit Newton method is used to solve the system of local constitutive equations. Switching to an explicit Runge–Kutta scheme with automatic time-stepping is possible when the Newton scheme does not converge in the presence of strong instabilities. The total number of degrees of freedom (DOF) is reported for all three cell: 91122 DOF for the square cell, 62130 DOF for the triangle cell, and 132742 DOF for the hexagon cell. Full-field finite element (FE) solutions are reported for the elastoplastic response of the three considered lattices considered. For each cell, the steel volume fraction is 30%. Selected FE results

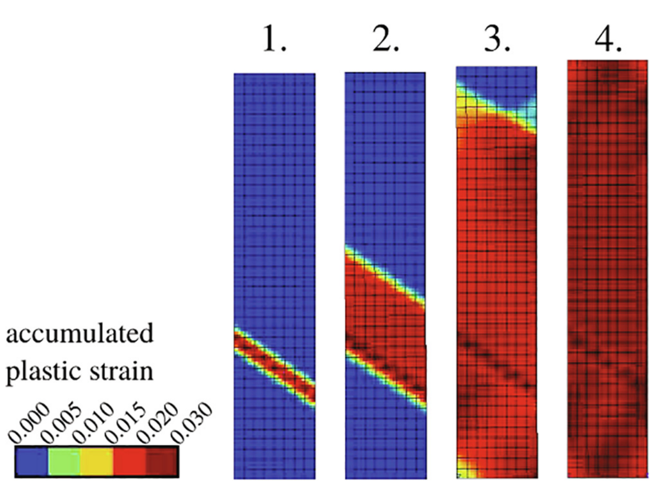

Fig. 4. Accumulated plastic strain map on a sample in tension with propagation of a Piobert-Lüders localization band.

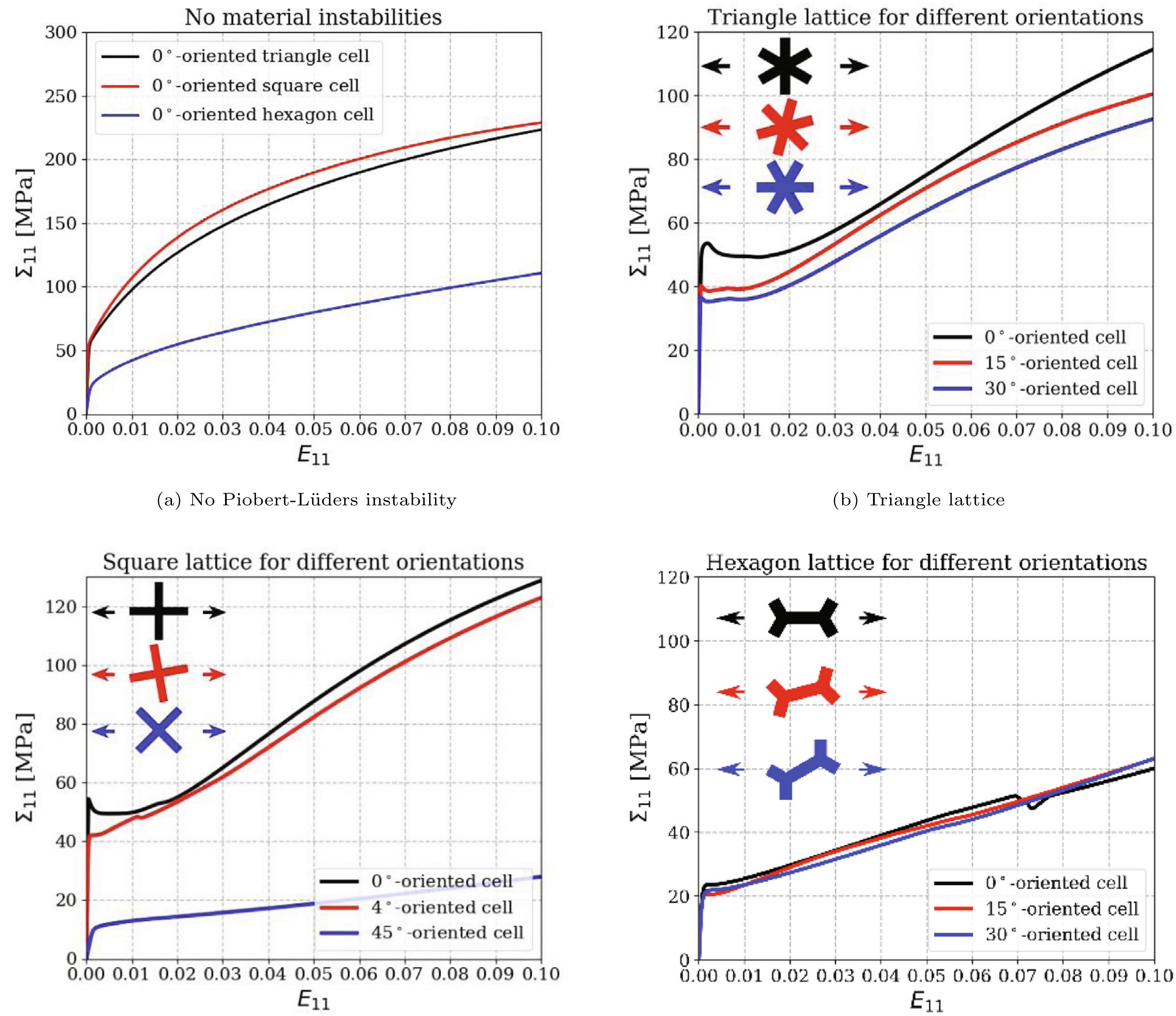

(a) No Piobert-Lüders instability

(b) Triangle lattice

(c) Square lattice

(d) Hexagon lattice

Fig. 5. Macroscopic stress-strain curve for studied lattices (a) without Piobert-Lüders instability (b, c, d) with Piobert-Lüders instability.

are reported up to a macroscopic strain of 10% and the accumulated plastic strain (*epcum* variable) evolution is given for most relevant orientations.

The macroscopic response of the three studied cells without Piobert-Lüders instability is reported in Fig. 5a for the most relevant orientation. The parameter Q_2 in the original behavior law (2) is changed to be positive with the same value. There is no localization in this case.

3.2. Triangle lattice

The macroscopic mechanical response of the triangular lattice has a global shape similar for all loading directions, see Fig. 5b. Stress levels differ depending on the orientation, from a plateau stress at 50 MPa for 0° to 35 MPa for 30°. The response exhibits an initial stiff and linear behavior corresponding to the elastic regime of the material. The stress reaches a first maximum value, a peak stress, when plastic strain localization starts. Then stress slowly decreases to reach a plateau, indicating that the propagation of plastic strain in the branches of the lattice has begun. Finally a hardening behavior takes place after the instability has finally crossed the whole structure. For the orientation 0°, the peak-plateau stress phenomenon is sharper. Besides, the triangular lattice is the only lattice to preserve the stress plateau in every loading direction due to its stretch-dominated behavior. The stress level for the plateau depends on the orientation of the lattice with respect to the loading direction.

The discrepancies of stress level and the local instability which occur for the three tensile tests can be explained through the analysis of the propagation of Piobert-Lüders instabilities within the triangle lattice. Figs. 6 and 7 represent the accumulated plastic strain for the triangle cell for two relevant orientations, 0° and 30°. Plastic localization initiates in the middle of the struts of the triangle. This nucleation depends on the orientation. For orientation 0°, plastic deformation starts in the two most loaded struts at the same time. For the other configurations, plastic deformation

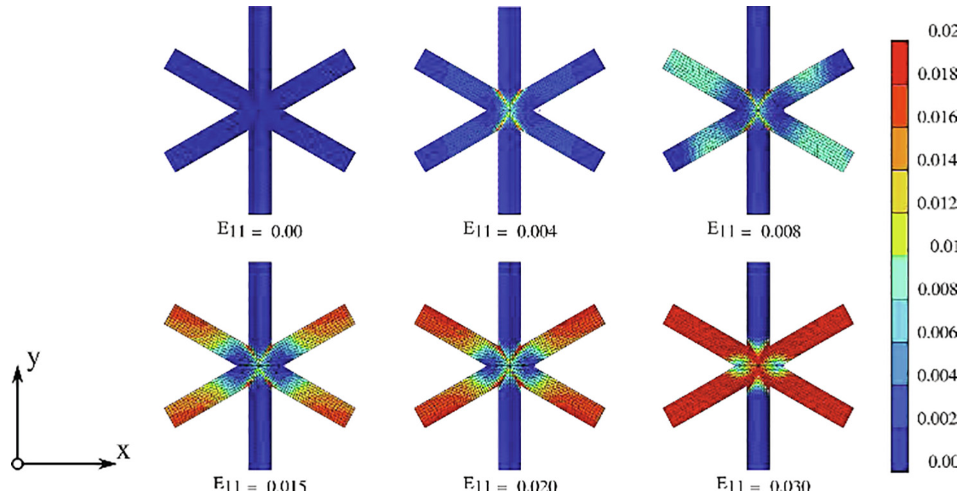

Fig. 6. Accumulated plastic strain map in the triangle lattice 0°-oriented unit cell.

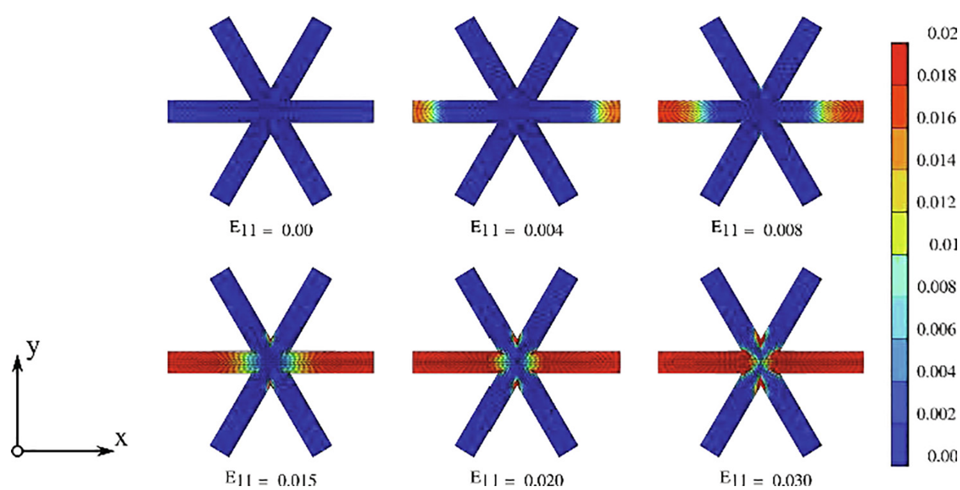

Fig. 7. Accumulated plastic strain map in the triangle lattice 30°-oriented unit cell.

begins, first, only in the best oriented strut with respect to the loading direction of the cell. Then, as the macroscopic loading increases, the plastic instability propagates along the struts symmetrically, see Fig. 7.

Because of the high-connectivity of the cell, the struts are mainly loaded in tension thus promoting the propagation of Piobert-Lüders bands. Whatever the loading direction, there are always struts subjected to tension. This results in a macroscopic behavior which exhibits a peak-plateau stress as the instability propagates throughout the lattice. The isotropic behavior of the triangle lattice is verified in the elastic domain while it is lost when plastic instabilities appear. The higher level of stress for the 0°-oriented triangle cell is due to the quantity of material that undergoes plasticity in the lattice. For this orientation in the end, 4 struts are plastic (see Fig. 6) while for the 30°-oriented cell there are only 2 (see Fig. 7).

3.3. Square lattice

Square lattice behaves very differently from the triangular lattice and both its linear and non-linear behaviors are strongly anisotropic. From the macroscopic stress–strain curves of the square lattice in Fig. 5c, two extreme mechanical responses can be identified. The first one, corresponding to the orientation 0°, is close to the localization-propagation behavior with a peak and a plateau stress. In contrast, the second one for orientation 45°, relies on the elastic then plastic bending of the struts and no peak nor plateau stresses are observed.

Therefore, the analysis of the square lattice is divided into three parts: stretching-dominated regime when struts are less than 5° misoriented with respect to the loading direction and a bending-dominated regime from 5° to 45°.

Stretching-dominated regime for 0°

Cell walls are exactly aligned with the loading direction. No mechanism is active in the lattice, neither bending of the walls nor plastic hinges. Conditions are close to a tension test on a single plate made of material undergoing Piobert-Lüders instability in Fig. 3 and 4. Three zones are identified from the macroscopic stress–strain curve in Fig. 5c:

Zone 1: Stress peak. The initial response of the lattice is linear until the yield stress is overcome while plastic strain localizes in the thickness of the strut. Unlike the plate in tension, no defect is needed to initiate the localization. Stress concentration in the lattice is enough to trigger localization in the loaded struts.

Zone 2: Stress plateau. The peak stress at 55 MPa is followed by a plateau at a stress level of 50 MPa corresponding to the plateau stress value for the triangular lattice at 0° and last until 0.02 macroscopic strain.

Zone 3: Hardening behavior of the lattice. After the Piobert-Lüders instability has propagated through the horizontal struts of

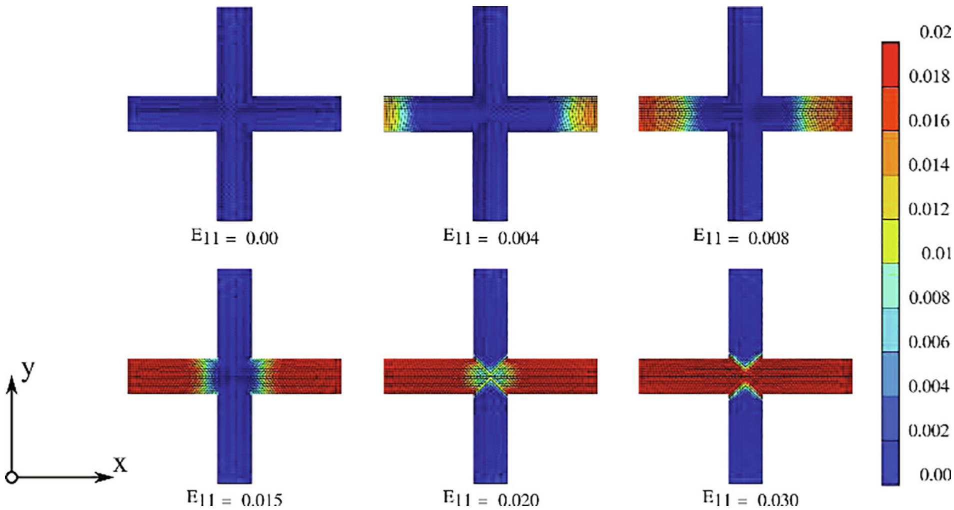

Fig. 8. Accumulated plastic strain map in the square lattice 0°-oriented unit cell.

the square lattice, the lattice undergoes a hardening behavior following the constitutive model.

Fig. 8 represents the accumulated plastic strain for the square cell at 0°. Localized plasticity initiates (zone 1) in the middle of the strut in tension into a single band. Then, it propagates along this strut (zone 2) until the whole strut is plastic and it reaches the central joint (zone 3). The localization does not take the shape of an inclined band as in the case of a sample in tension. The transverse struts of the lattice connected with periodic boundary conditions prevent the strut with plastic localization to accommodate the macroscopic deformation. None of the two inclined possible bands is favored so they both coexist.

Stretching-bending regime for 4°

The unit cell is now slightly rotated from the tensile loading direction. The strut oriented at 4° is loaded in both tension and bending. The macroscopic behavior of the 4°-configuration in Fig. 5c is compared to the 3 steps of 0°-configuration.

Zone 1: Elastic bending of the struts. The FE analysis captures the elastic bending of each strut. The effective Young modulus depends on the orientation of the strut with respect to the loading direction, which shows the anisotropy of the square lattice in elastic regime. An analytical expression is given by Gibson and Ashby (1999). Compared to the 0°-oriented cell, there is no peak in this case. Because the strut is bent, stress along the strut depends on the lever arm from the end of the strut. This is unlike tension where the stress is uniform until plasticity occurs.

Zone 2: Plastic bending of the struts. Plasticity propagates in the struts of the cell and elastic bending becomes plastic bending. As a result of the variable stress, the stress plateau is replaced by an increasing stress until 0.12 macroscopic strain.

Zone 3: Hardening behavior of the lattice. As for the 0°-oriented lattice, the lattice undergoes a hardening behavior after a local instability marking the end of the propagation phase.

The accumulated plastic strain map of the square cell oriented at 4° is represented in Fig. 9. While struts undergo elastic bending (zone 1), plasticity starts early in the corners at the joints where stress concentration is maximum on the side in tension. From there, localized plasticity propagates towards the border in tension of the bent struts. Plastic instability propagates along the half strut under tension (zone 2) until it is fully plastic. When the band

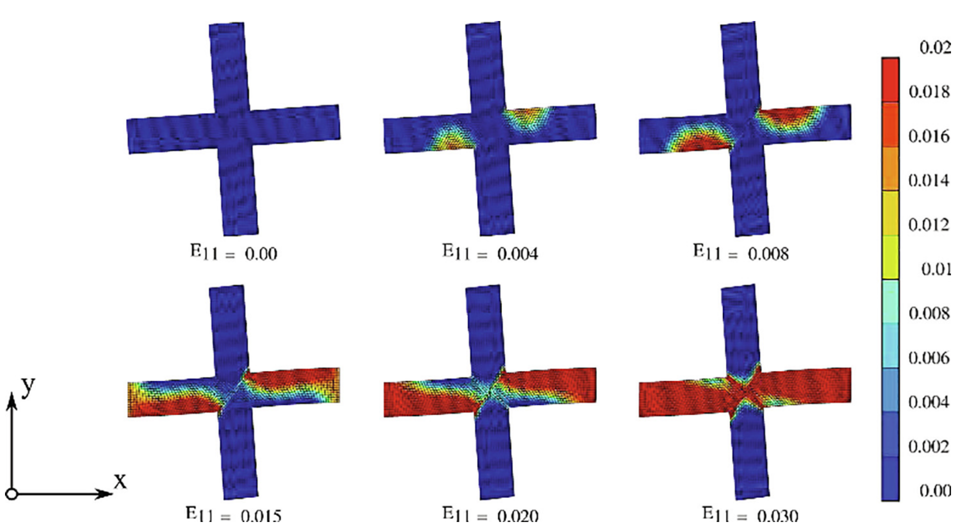

Fig. 9. Accumulated plastic strain map in the square lattice 4°-oriented unit cell.

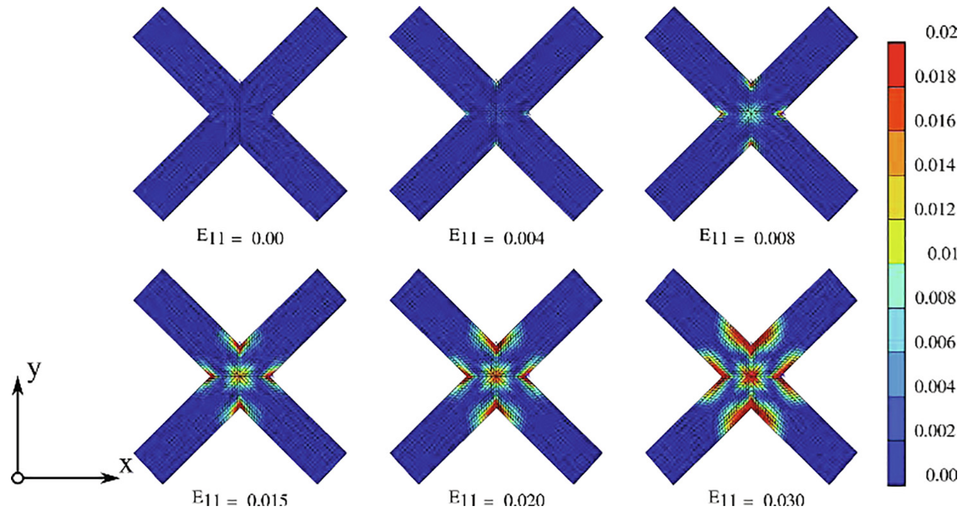

Fig. 10. Accumulated plastic strain map of the square lattice 45°-oriented unit cell.

reaches one end of the strut, it continues in the second half which has not yet fully reached plasticity (zone 3).

Bending-dominated regime for 45°

In the case of the square cell oriented at 45°, the macroscopic behavior of the lattice is two-fold (see Fig. 5c). First, the response is linear with an effective Young modulus lower than for other orientations. Then, the lattice enters the elastoplastic regime and hardening takes place.

The accumulated plastic strain maps of the square cell oriented at 45° are represented in Fig. 10. While struts undergo elastic bending, plasticity initiates early in the corners at the joints where stress concentration is maximum. From there, localized plastic strain spreads but is still confined at the joints. Plasticity never propagates through the struts. Neither a peak nor a plateau can be seen on the macroscopic stress–strain curve. As the Young modulus increases when the struts tend to align with the loading direction, the plastic behavior of the square lattice evolves gradually from the 45°-oriented cell to the 5°-oriented one.

The orientation of the square lattice modifies its mechanical behavior from stretching-dominated to bending-dominated but it also inhibits the propagation of Piobert-Lüders instabilities. In stretch-dominated configuration, the square cell exhibits a propagative behavior for plastic instabilities following the peak-plateau stress response observed for the triangular lattice. On the contrary, the bending-dominated configurations exhibit a hardening behavior without propagation of plastic instabilities.

3.4. Hexagonal lattice

The comparison of the macroscopic behavior of the hexagon cell oriented at 0°-degree with Piobert-Lüders instability and without, respectively Fig. 11 and 5a, highlights the effect of the softening in the plastic region.

The in-plane isotropic behavior of the hexagonal cell in elasticity is verified while the behavior with plastic instabilities become anisotropic. Because of the low connectivity of the hexagonal cell, this lattice acts like a mechanism, *i.e.* it is bending-dominated. After an isotropic linear response of the material, deformation becomes plastic. The global behavior of the hexagonal lattice depends very little on the orientation. The macroscopic stress–strain curves for 3 relevant orientations in Fig. 5d differ only slightly in the plastic domain. The behavior is characteristic of bending–dominated lattices. For the 0°-oriented cell, a stress drop is observed at 0.07 macroscopic strain. It is caused by Lüders localization in the single stretched strut. No stress plateau is observed.

It is found that no propagation of the Piobert-Lüders instability can be observed in the hexagonal lattice whatever the direction of loading, except for the 0°-orientation (see Fig. 11). For this orienta-

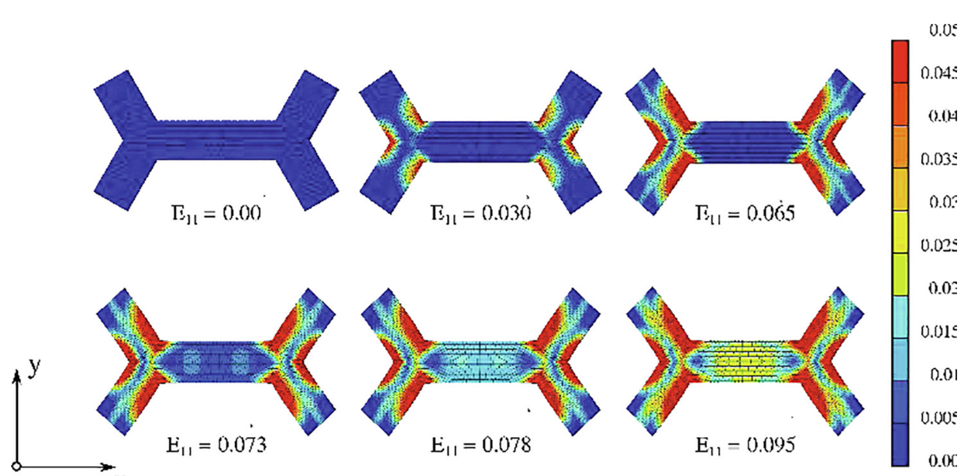

Fig. 11. Accumulated plastic strain map of the hexagon lattice 0°-oriented unit cell..

tion, some struts are aligned with the tensile direction and a Piobert–Lüders band can form. This occurs at the same overall stress level of 55 MPa as for the square and triangular lattices. However the propagation remains limited, see Fig. 11, so that no extended plateau is observed on the overall curve. Due to low connectivity, the inner mechanism, inducing the bending-dominated behavior of the hexagon, does not activate the propagation of Piobert-Lüders instabilities regardless of the orientation.

A two-fold behavior, propagative or non-propagative, has been identified for 2D periodic lattices characterized by their either stretch- or bending-dominated mechanical behavior. Moreover for each lattices, discrepancies appear in the plastic behavior instabilities due to different orientations. This validates that plastic instabilities can be modified using both architecture and orientation. The propagative behavior of Piobert–Lüders bands can be altered depending on the 2D lattice structure and loading direction. The propagation of Piobert–Lüders bands along the struts of the lattice is found to take place mainly in stretch-dominated lattices provided the struts are properly oriented with respect to the loading.

4. The role of the number of unit cells

It is well-known that the analysis of the stability of periodic structures cannot be limited to the study of a single unit cell. This is due to the fact that instability modes can emerge, exhibiting a wavelength larger than the unit cell size (Triantafyllidis and Bardenhagen, 1996; Schraad and Triantafyllidis, 1997). It is necessary to examine a larger volume element (VE) composed of more that one primitive unit cell. It means that the periodic boudary conditions (PBC) are no more imposed on a single unit cell but on the boundary of the larger volume element. Simulations of the previous section were carried out again for VE sizes of 3×3 and 5×5 cells, named respectively 9-cell RVE and 25-cell RVE in the following. In Fig. 12 the macroscopic curves are plotted for

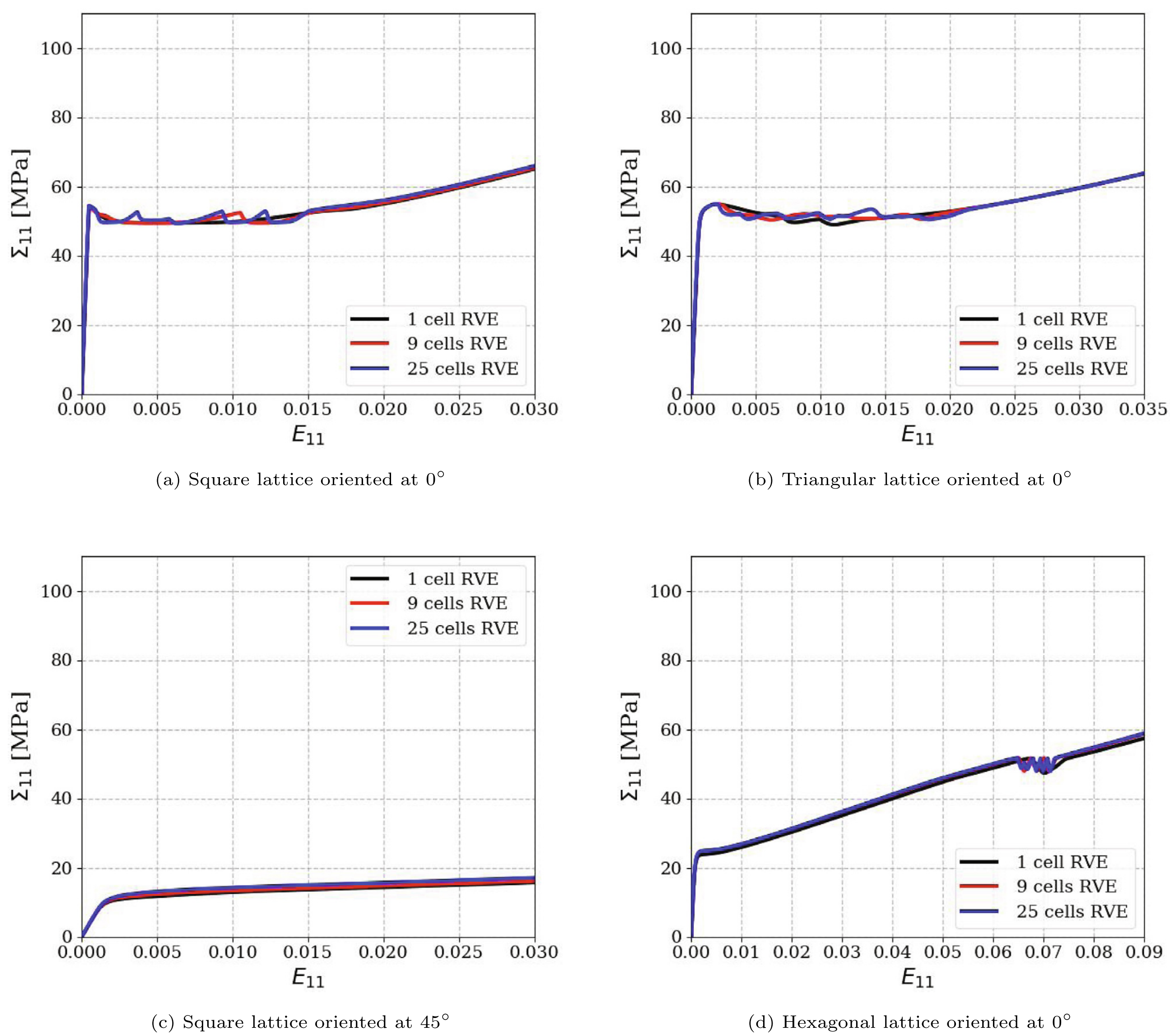

Fig. 12. Macroscopic behavior of RVE with increasing number of cells.

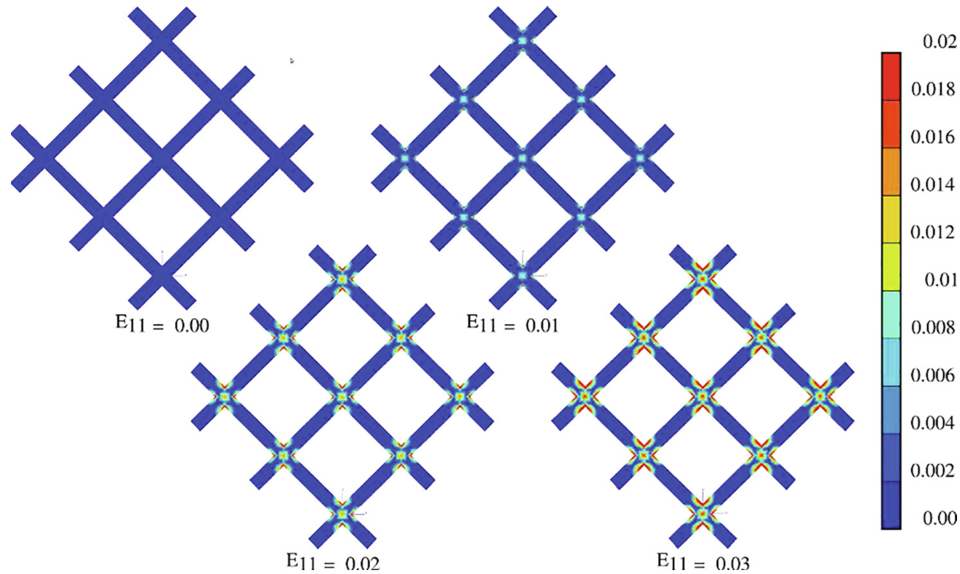

Fig. 13. Plastic strain map in a 9-cell 45°-oriented square lattice.

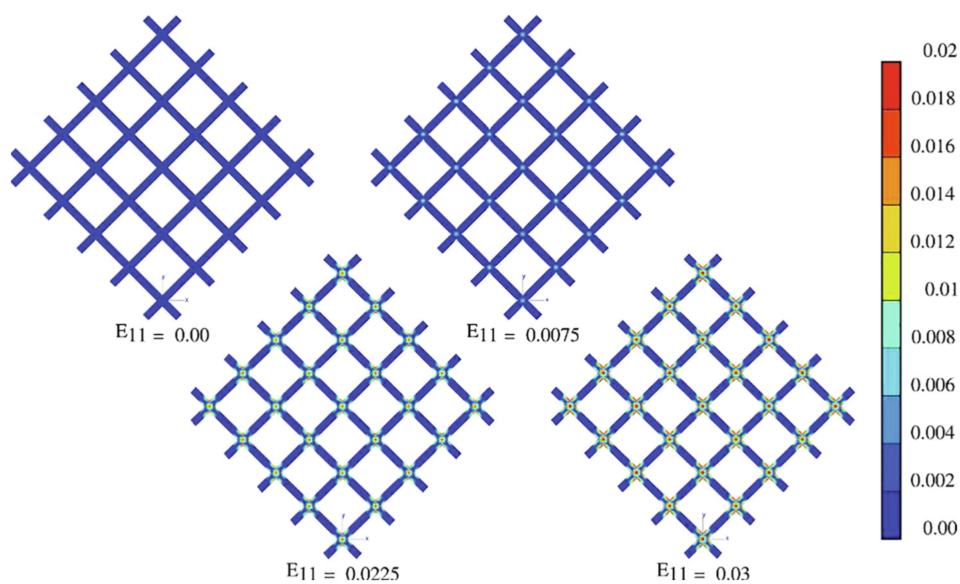

Fig. 14. Plastic strain map in a 25-cell 45°-oriented square lattice.

the square lattice with the orientations 0° (a) and 45° (c), for the 0°-oriented triangular (b) and hexagon (d) lattices. For bending-dominated lattices as well as the 45°-oriented square and hexagon, no discrepancy is observed between the one-cell and multiple cell VE responses (see Fig. 13 and 14). In the case of propagating instabilities during the loading of the lattice (stretched-dominated or square 0°-oriented), differences can be observed only when instabilities cross the whole lattice (Figs. 15 and 16). During the phase of instability propagation, localized plasticity occurs in the struts in tension. Then two possible patterns of localization exist: as in Fig. 16 at $E_{11} = 0.003$ where the five struts of a single column undergo plastic deformation or in Fig. 16 at $E_{11} = 0.0045$ where the plastically deforming struts are distributed on two columns. This cell to cell propagating behavior also occurs for the hexagon cell oriented at 0° in Fig. 19 in the horizontal struts. Macroscopically, the number of columns in the RVE, for example 5 for the 25-cell RVE, matches the number of stress drops on the macroscopic curve of Fig. 12 (d) which corresponds to the sequential localization of the stretched struts in each column. Once the plastic instabilities have propagated through the whole lattice structure, the global behavior is identical whatever the size of the RVE. The same conclusions are drawn for the triangular and hexagon lattices both also simulated with 9 cell and 25 cell RVE which are respectively stretched-dominated and bending-dominated. The global behaviors of these lattices are reported in Fig. 12 (b) and (d). The accumulated plastic strain maps are reported in Fig. 17–19.

Piobert-Lüders instabilities in periodic media are found to be non-propagative for bending-dominated lattices. Each cell undergoes the same mode of plastic strain localization. On the contrary, stretched-dominated lattices exhibit propagating localization through the lattice while two neighboring cells do not undergo the same plastic strain localization during the propagation stage. Moreover in those last lattices, several modes of localization exist involving one or more columns of struts perpendicular to the loading direction. Changing the definition of the RVE changes the instability propagation mode. A primitive RVE does not capture all

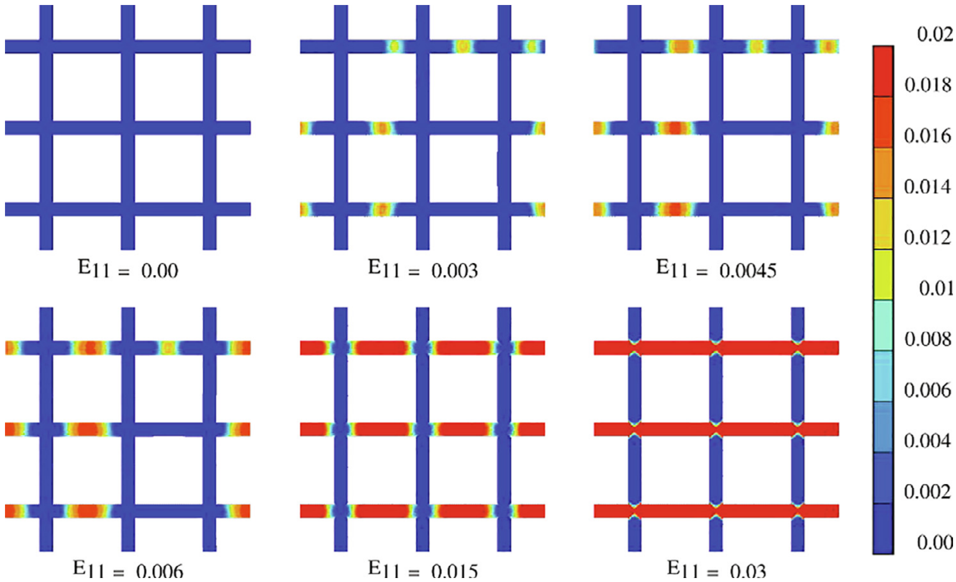

Fig. 15. Plastic strain map in a 9-cell 0°-oriented square lattice.

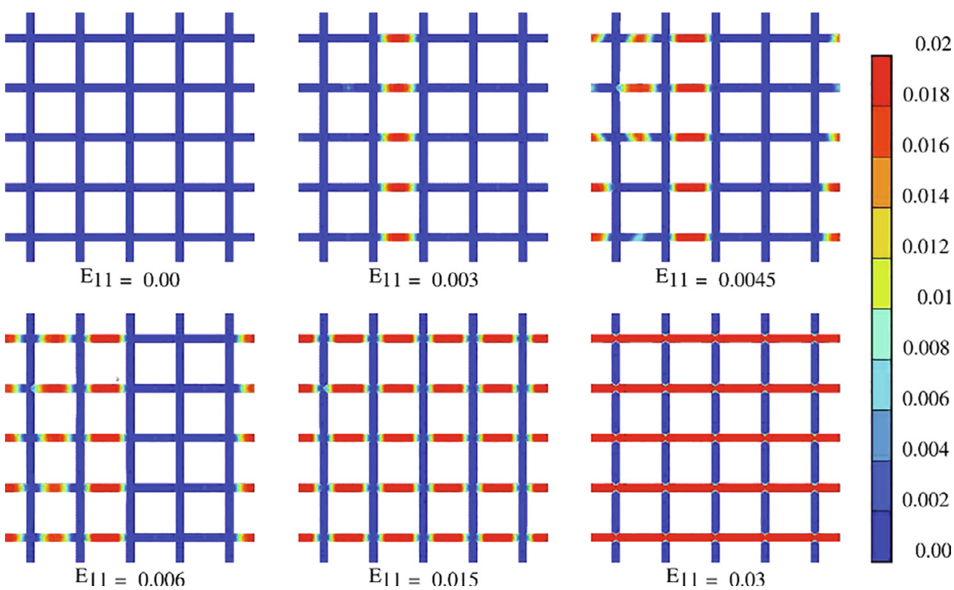

Fig. 16. Plastic strain map in a 25-cell 0°-oriented square lattice.

possible modes of localization for material instabilities. New modes with two columns of tensile struts involved in the propagation of instabilities are highlighted with higher number of cells in the RVE. By increasing the size of the RVE, constraints on the cells are relaxed compared to the primitive cell RVE.

5. Experimental analysis

A comparison between the numerical model and experimental results is proposed in this section. The two specific types of lattice behavior, namely bending-dominated and stretch-dominated, with propagating material instabilities have been tested in tension. In order to understand the propagation of Piobert–Lüders bands in those lattices, different specimens have been architectured by laser cutting of steel sheets. The three same geometries as for the numerical study are chosen: the triangle, square and hexagon. Those lattices are representative of the mechanical behavior of the archetypal bending- and stretch-dominated behaviors. The dimensions of the samples are limited by two opposite constraints. On the one hand, the number of cells must be large enough to allow for a description of the transmission of local to global instabilities. On the other hand, strain field measurements are necessary for quantitative analysis of the structural response at the strut level. Due to these experimental constraints, a relative density equal to 50% has been retained. Struts have to be thick enough to track the localization by means of Digital Image Correlation (DIC). The total number of cells is limited to ensure that observations of global and local strain fields are simultaneously possible. The specimens used for the experiments are shown in Fig. 20. Finally, the relevant dimensions for the samples are the total width of 2 cm and the total length of 8 cm. The thickness of the specimens is 1 mm. For the square cell, the width of a strut is 1.5 mm and its length 3.45 mm. For the triangle cell, the width of a strut

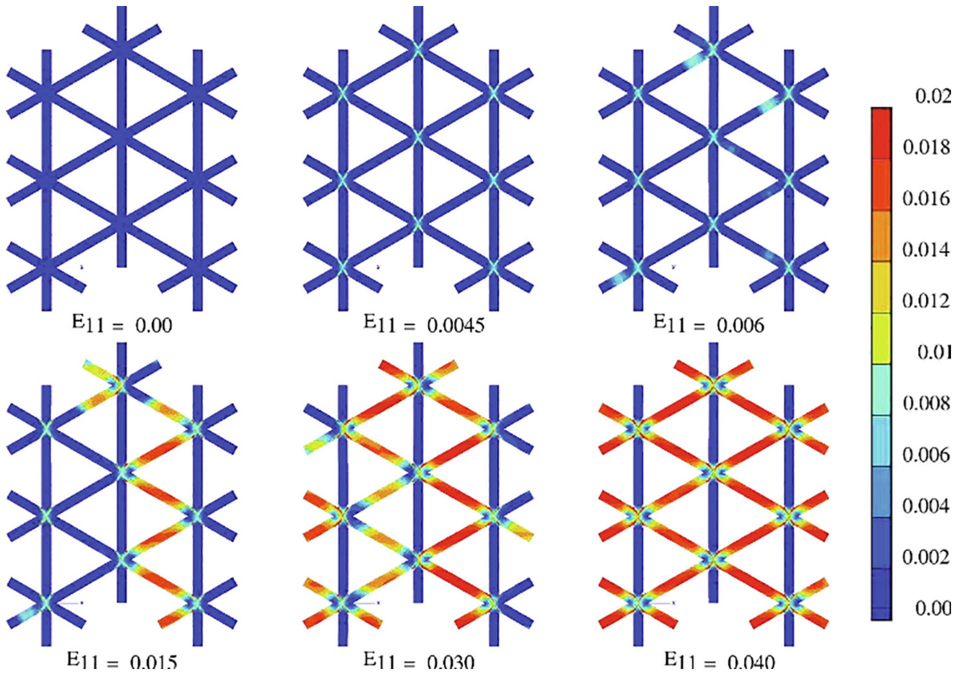

Fig. 17. Plastic strain map in a 9-cell 0°-oriented triangle lattice.

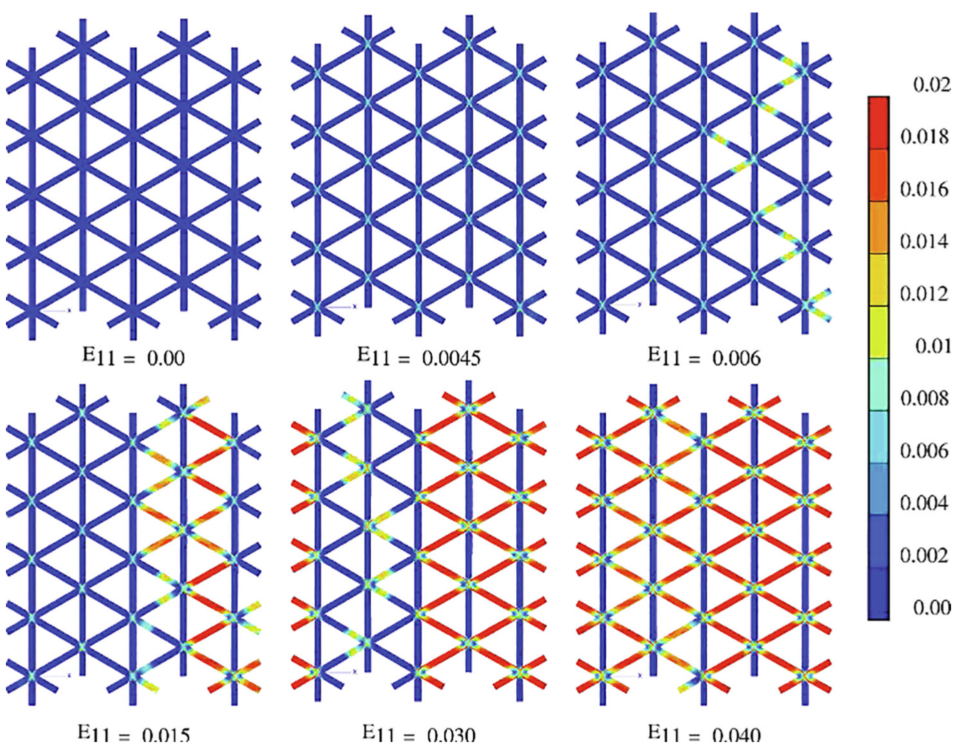

Fig. 18. Plastic strain map in a 25-cell 0°-oriented triangle lattice.

is 1.5 mm and its length 5.3 mm. For the hexagon cell, the width of a strut is 1.8 mm and its length 2.8 mm. Fig. 21 shows the sample at the end of the experiment.

The investigated material is an ARMCO® low carbon steel alloy. ARMCO® steel is know to be very sensitive to static strain ageing. It exhibits the Piobert-Lüders phenomenon. Table 3 provides the chemical composition of the experimented material for additional elements to a 99.85% Fe base.

5.1. Digital image correlation

Experiments are conducted on a MTS-10t servo-hydraulic tensile machine. The load cell measuring range is 0 – 100 kN. No extensometer was used due to the heterogeneous architecture of the samples. Digital Image Correlation (DIC) displacement field measurements were performed instead. The main features of the DIC set-up are: Dual camera system: 4.1 Mpixels each (Manta

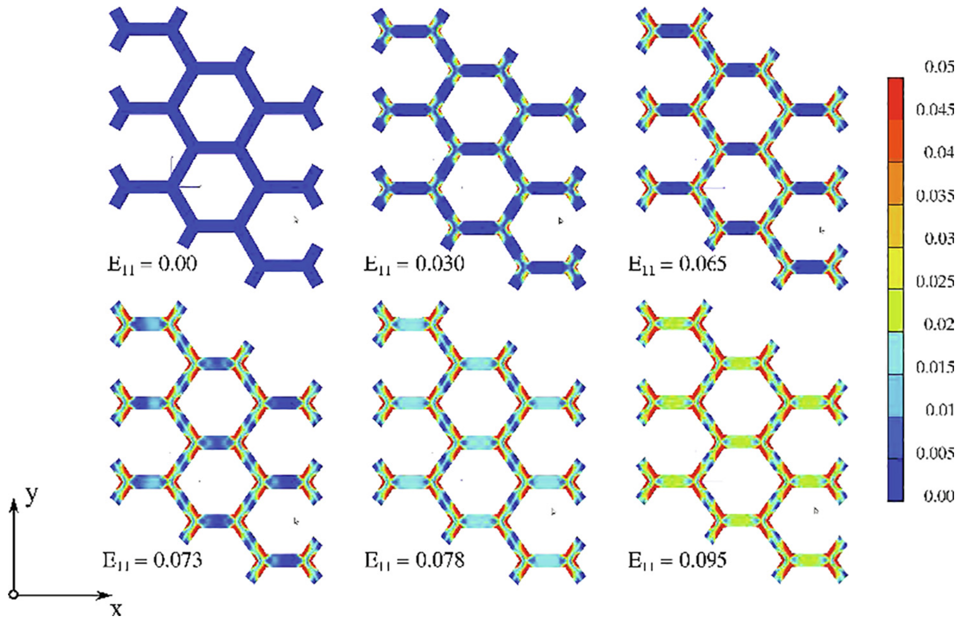

Fig. 19. Plastic strain map in a 9-cell 0°-oriented hexagonal lattice.

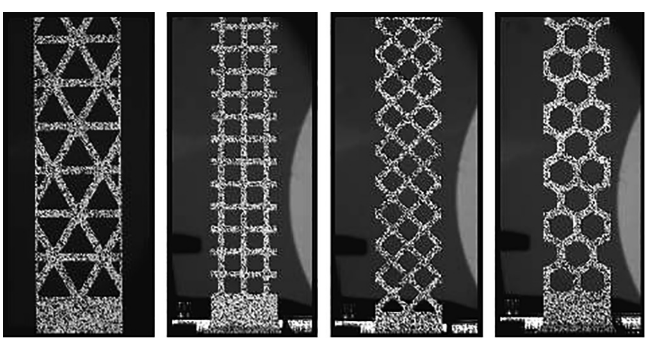

Fig. 20. Speckled architectured samples for experimental comparison.

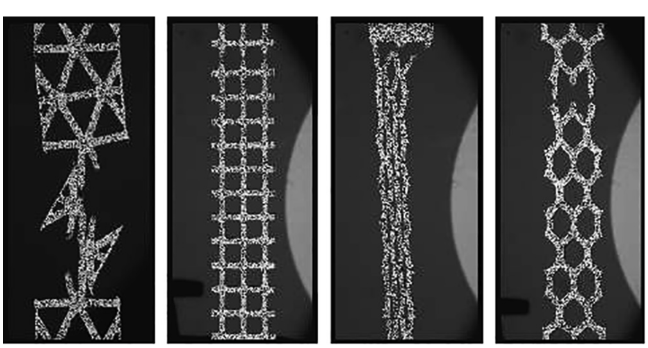

Fig. 21. Speckled architectured samples broken after testing.

G419) with a maximum frequency acquisition of 27 images/s in high resolution and correlation software VIC-3D. The experimental set-up is shown in Fig. 22.

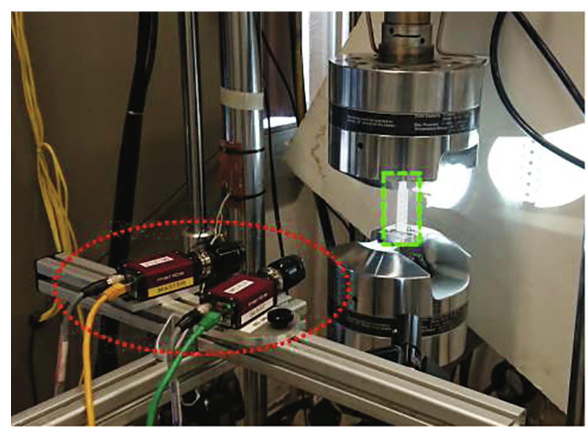

Fig. 22. Experimental set-up for digital image correlation. In red: cameras system, in green: tensile specimen.

The full-field surface displacement of the sample is computed from a random pattern tracked during the experiment. A subset is a collection of pixels values identified on the undeformed sample. The unique grayscale pattern associated to this subset is its signature. The correlation algorithm tracked this subset on every image of deformed sample taken during the experiment. Identification is made using a criterion of maximum similarity with the reference image. Another possible strategy is updating the reference image by the $n-1$ image. The random pattern is obtained by spraying painting on the specimen surface.

Measurement uncertainty is evaluated by correlating two repeatedly acquired images without rigid body motion. The error on the strain field is mainly due to the numerical noise of the cameras. The minimum strain between two images must be more than the strain resolution calculated this way.

Table 3
Chemical composition of ARMCO steel provided by the steel manufacturer.

	C	Mn	P	S	Cr	Cu	N	Ni
Chemical composition [wt%]	0.02	0.050	0.004	0.0027	0.017	0.007	0.005	0.016

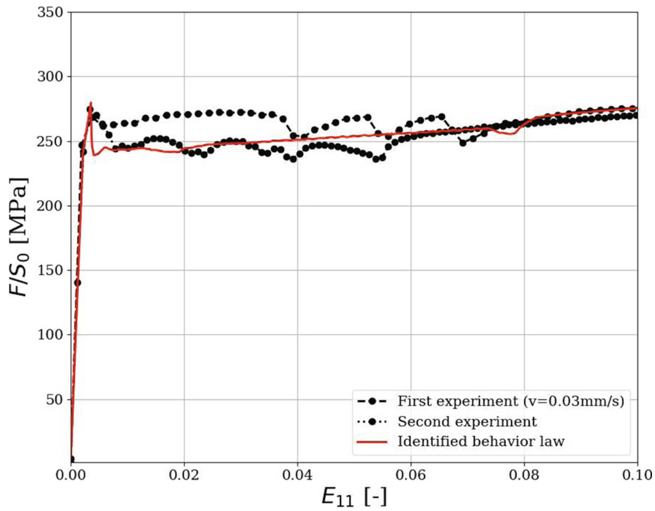

Fig. 23. Tensile test response of a sheet material with propagation of plastic instabilities and comparison with the identified model of Section 2.

5.2. Experimental results

Identification. Fig. 23 shows the tensile response of the plain strip of steel subsequently analyses in Fig. 24. The effect of the propagation of plastic instabilities is clearly identifiable on this curve through the peak and plateau stress. The identification of parameters for the model is delicate. Three features are important to replicate in this study. Since we are interested in the propagation of instabilities, it is important to model properly the peak and the entire plateau stress. The two experimental curves obtained in the same conditions highlight the complexity of identifying a single set of parameters. We focused on capturing the strain of the peak and the rough stress level of the plateau with its length. The after-plateau behavior is easily identifiable. Parameters are given in Table 4.

Table 4
Experimentally Identified parameters for the phenomenological plasticity model.

R_0 (MPa)	Q_1 (MPa)	b_1	Q_2 (MPa)	b_2	Q_3 (MPa)	b_3
259	360	33	−360	55	30	2000

Numerically, this set of parameters which fits with the experiments introduces a premature necking after the end of the plateau. This is due to the stress level of the peak which is too close from the stress level plateau.

Piobert-Lüders instability propagation in the sheet material. A reference test has been performed for the initial sheet material, *i.e.* without any inner architecture. The objective is to characterize the Piobert-Lüders bands in the bulk material. Strain localization is found to occur at one end of the sample in tension in the form of two symmetrical bands as shown in Fig. 24 (b). Then, the two bands propagate all along the sample and reach the other end. Fig. 24 (c) shows that after the passage of the band the strain level

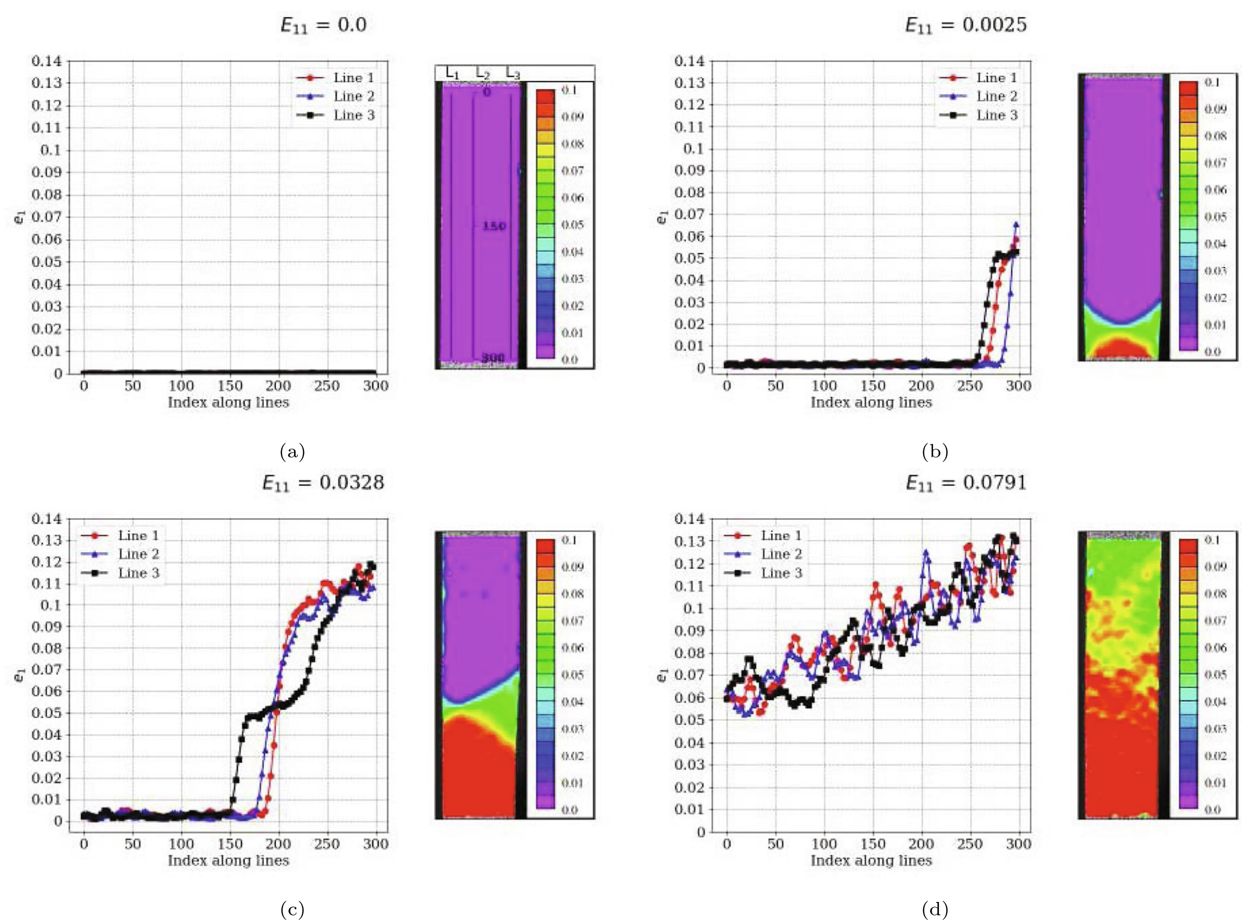

Fig. 24. Bulk sheet in tension with propagation of Piobert-Lüders instability with digital image correlation results. On the left is represented the strain e_1 in the tensile direction for three different lines defined on Figure (a). On the right is represented the map obtained by DIC of the strain e_1.

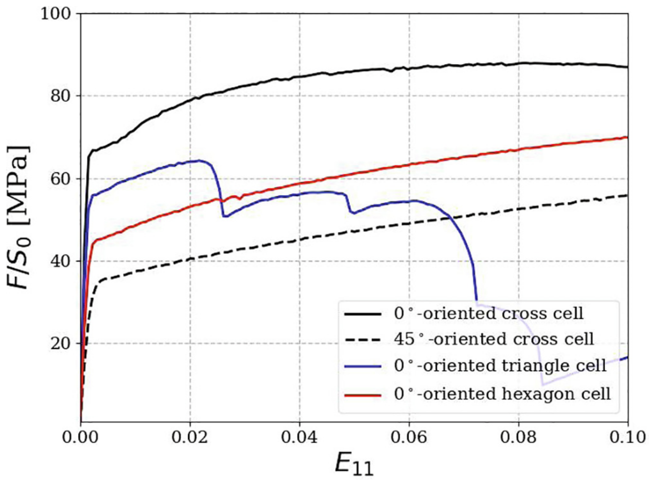

Fig. 25. Experimental stress–strain curves of architectured samples.

is about 10%. In the band front, the strain level ranges between 5% and 6%. The band front width is between 0.8 cm where the two bands crossed and 1.2 cm at the largest. Once it passes the middle of the specimen, the front band is not clearly defined any more and strain levels spread from 7% to 14%. This experiment on a bulk sample allows us to characterize the propagation mode of the instability without interaction with any architecture and will be necessary for the identification of the model later on. The reader is referred to Mazière et al. (2017) for a direct comparison of numerical and experimental results in the case of a C-Mn steel.

The tensile curve for the architectured samples is given in Fig. 25. The macroscopic strain E_{11} is computed for the machine displacement divided by the initial length of the sample, 8 cm. The strain is calculated from the force divided by the total initial section, $S_0 = 1 \times 15$ mm. This definition for the strain does not take into account the architecture since it is not possible to define a unique section along an architectured sample. For each oriented architecture, 3 samples have been tested. The results are very comparable (less than 5% differences on the overall curves) so only one response of each sample is reported in Fig. 25.

Stretch-dominated behavior for a square lattice oriented at 0°. In the case of the square at 0°, localized plasticity starts in the middle of the struts under tension. During this regime, the activation of plasticity in each strut occurs in a random way until they all reach the same level of accumulated plastic strain, see Fig. 26 (a) and (b). After plasticity has been activated in all the struts, Piobert–Lüders bands propagate along the strut until accumulated plastic strain value of 0.06 is reached in every strut, as shown in Fig. 26 (c). We demonstrate with this 0°-oriented square lattice specimen that, in stretch-dominated lattices, plasticity initiates first in the struts in a random manner, i.e. all struts do not become plastic at the same time. Material instabilities are globally propagating through the lattice. Locally, the propagation of plastic instability in single struts is not easily visible. This is likely due to the width of the localization band front being larger than the struts.

In addition, side effects can be observed in snaps of Fig. 26 (c), struts in the middle column behave differently that the ones on

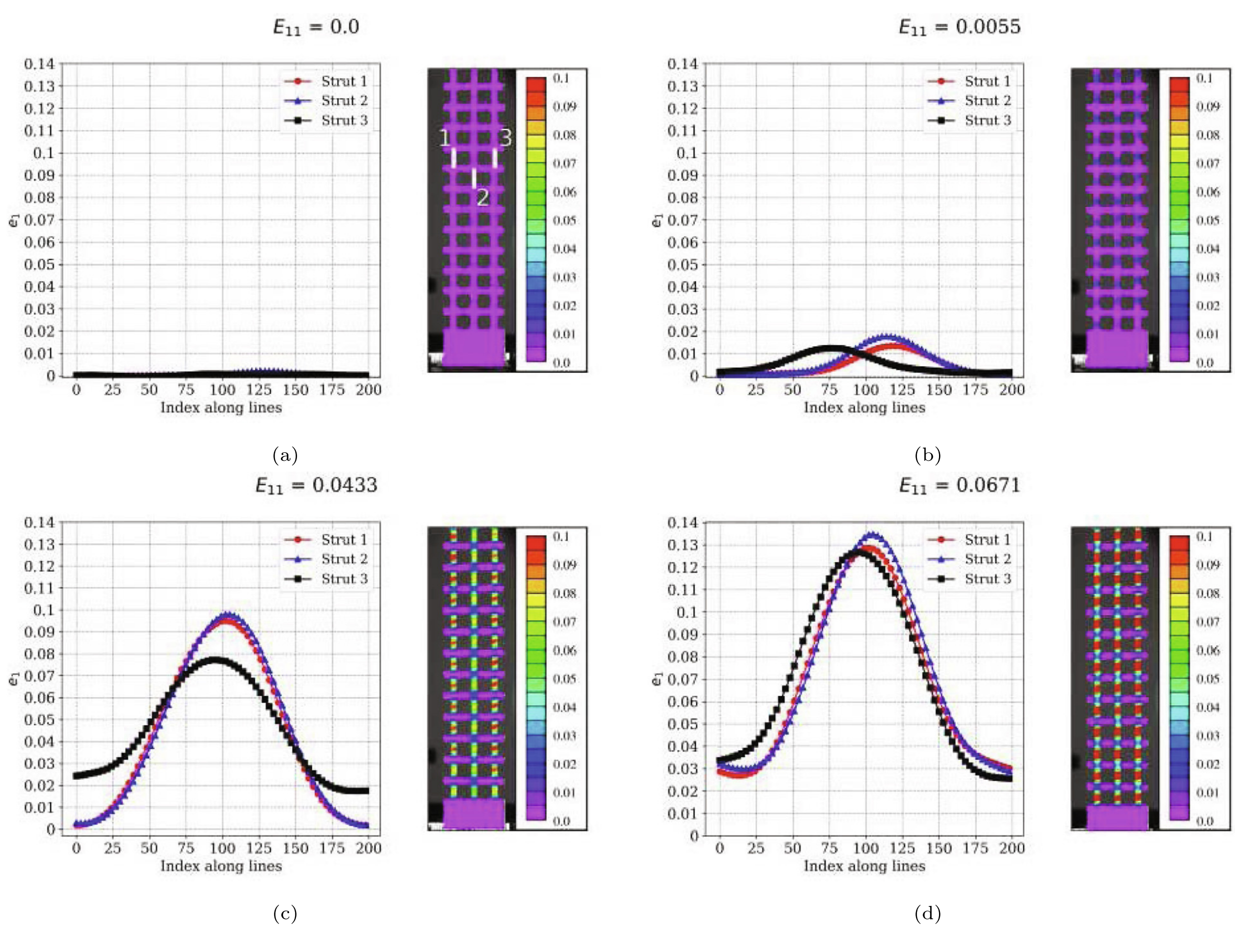

Fig. 26. Architectured sample with 0°-oriented square architecture loaded in tension. On the left-hand side is the strain in the loading direction for three different struts represented in (a). On the right-hand side is the map of the strain in the loading direction, e_1, computed from image correlation measurements.

the edges. In the middle, plasticity propagates through the nodes of the lattices while for the ones on the edges plastic strain increases up to 10%. Finally, strain equalizes in all struts. Moreover, in a strut the localized plastic strain does not have sufficient space to propagate as a band. The localization zone occupies one half of the struts. This effect can be modified by designing cells with longer struts.

Bending-dominated behavior for a square lattice oriented at 45°. In the case of the square at 45°, plasticity localizes in the nodes of the lattice. In contrast to the 0°-oriented lattice, there is no random localization regime. We observe essentially the same distribution of strain along three different struts and also on the strain map on the right side in every struts. No global band propagation at the scale of the lattice can be observed. The level of strain rises in the same way in all cells at the same time.

We demonstrate that for a bending-dominated lattice, there is no material instability propagation through the lattice. Plasticity develops in all cells at the same time. Edge effects are less significant than for the specimen with 0°-oriented lattice. Fig. 21 shows a comparison between specimens before tension and after failure. It also underlines the limitations of such testing. On the square oriented at 45°, cells that break do not undergo the same boundary conditions than those in the middle of the sample. Those cells have some struts that are not connected. For the hexagon, cells on the edge have only one neighboring cell, thus their deformation is different from the ones in the middle of the sample. For a more complete analysis, it would necessary to consider larger samples by adding more cells in the specimen. In the case of the triangular lattice, premature failure of some struts modify the connectivity of the lattice, and, consequently the mechanical behavior and the propagation of instabilities.

The question of the number of cells that are necessary in both X and Y directions to estimate quasi-perfect periodic boundary conditions remains open.

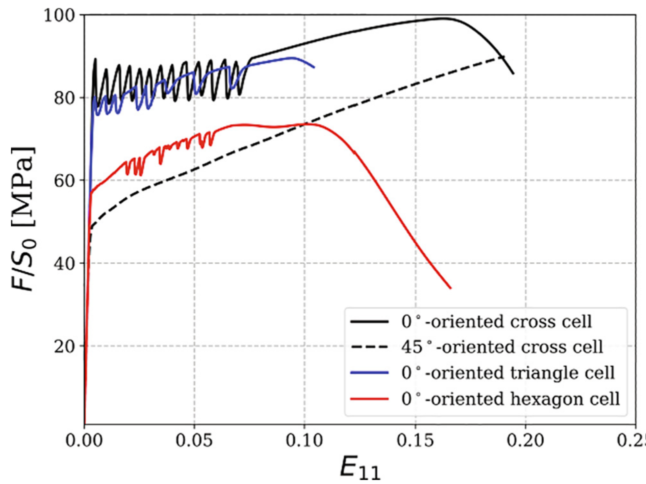

Fig. 28. Simulation of the architectured samples: stress–strain curves.

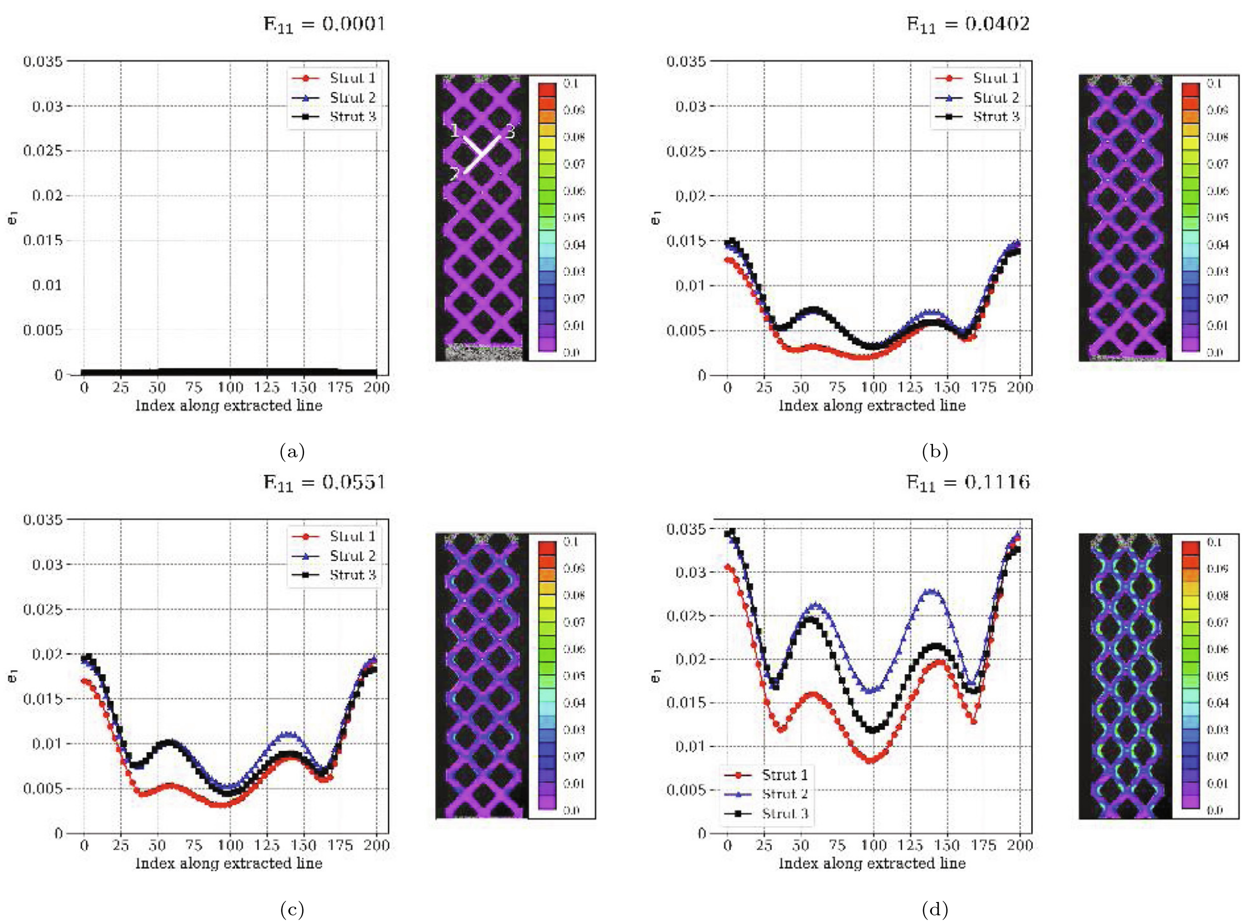

Fig. 27. Architectured sample with 45°-oriented square architecture loaded in tension. On the left-hand side is the strain in the loading direction for three different struts represented in (a). On the right-hand side is the map of the strain in the loading direction, e_1, computed from image correlation measurements.

5.3. Finite element modeling of the experiments

From the identification of the parameters we can simulate the experiments on the architectured samples. The calculations are performed within the large deformation framework with quadratic triangular elements with reduced integration (6 nodes and 3 Gauss points). Finite element meshes of the 4 samples of Fig. 20 were built and used for the simulation of their structural behavior in tension. Numerical samples are 3D. Fig. 28 shows the mechanical tensile response of the 4 tested architectured samples: triangle, hexagon, square loaded at 0° and square loaded at 45°. The ranking of the 4 architectures is found to be in good agreement with the experimental curves of Fig. 25. From the strongest to the weakest responses, we observe: the 0°-oriented square lattice, the triangular lattice, the hexagon lattice and the 45°-oriented square lattice. The simulation results overestimate the stress levels for all 4 architectured, by 15 to 20%. In the Fig. 25, the initial apparent Young modulus is found to differ for all four lattices. The numerical model confirms the theory with Young moduli equal to 94 GPa, 16 GPa and 26 GPa respectively for the square at 0°, the square cell at 45° and the hexagon 0°.

For each stretched- or bending-dominated architectures, the observed behavior of plastic instabilities is in accordance with the numerical predictions. For the 0°-oriented square cell and the triangle cell, we observe the plateau stress even though it is less pronounced in the experiment. The numerous drops in the simulation correspond to the localization/propagation phenomenon in each strut of the lattice. In the case of the 0°-oriented square cell, localization occurs in each row of the strips one after another. In contrast, in the 45°-oriented square and the hexagon samples there

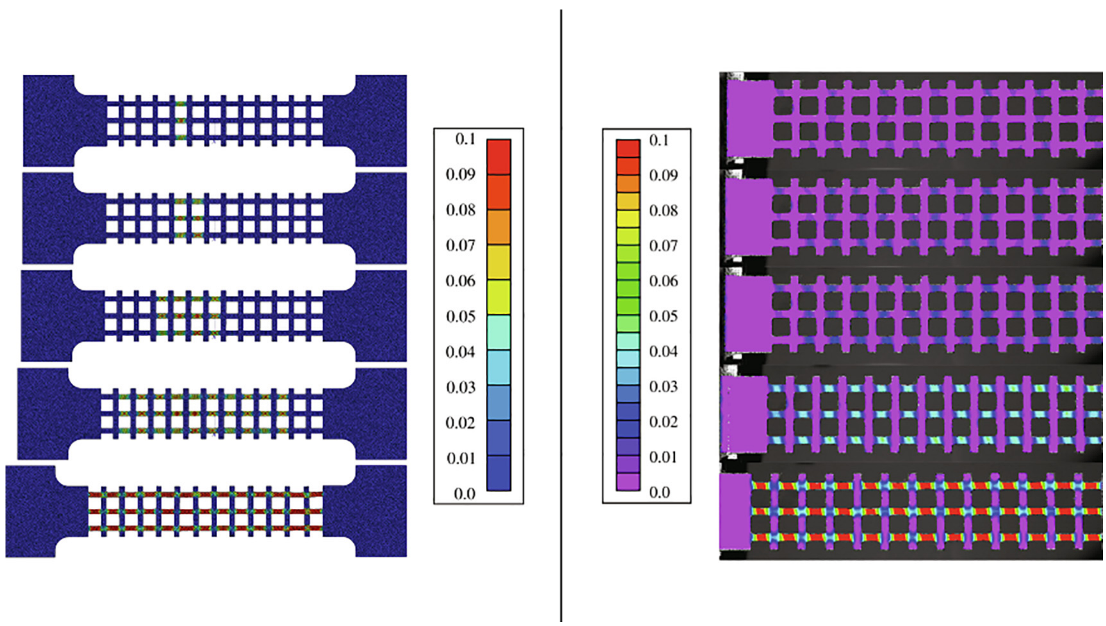

Fig. 29. e_1 strain map in the tensile direction for the 0°-oriented square lattice with comparison of the simulation on the left to the experiment on the right.

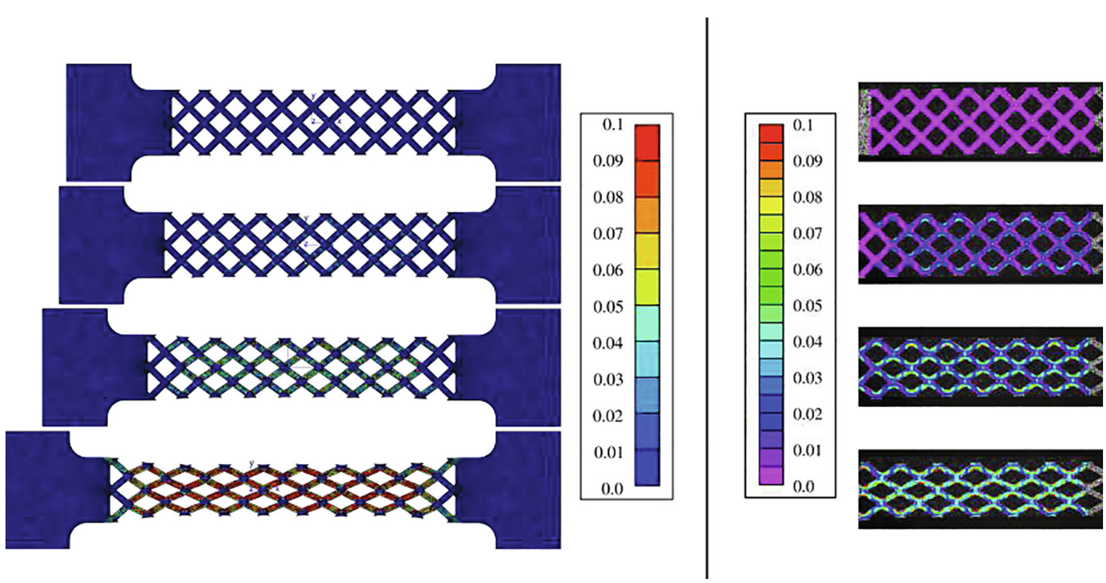

Fig. 30. e_1 strain map in the tensile direction for the 45°-oriented square cell with comparison of the simulation on the left to the experiment on the right.

is no macroscopic manifestation of the propagation of plastic instabilities as predicted by the periodic FE model. The hexagon simulation in Fig. 28 highlights load drops not visible in the experiment. In the simulation, those drops are the results of a plastic localization in the struts oriented in the direction of the loading.

The decrease of the stress after more than 10% overall strain in the simulation curves of Fig. 28 is due to premature necking of the struts, which differs in the experiment. However, this premature necking after the end of the stress plateau or after the propagation of plastic instabilities does not impact the understanding of the propagation modes of instabilities.

The plastic strain maps of Figs. 29 and 30 show comparisons between the experiments and simulation for e_1, the local strain in the tensile direction. They confirm the different scenarios of Piobert–Lüders band propagation between stretch- and bending-dominated lattices, deduced from the computational homogenization analysis. In the two stretch-dominated lattices, we observe propagation of strain localization bands at the two scales: the scale of each unit cell and the scale of the whole lattice structure. The propagation of a macroscopic horizontal localization band is clearly visible on the left side of Fig. 29. This is also the case in the experiment, see the right side of Fig. 29, but to a lesser extent, meaning that several horizontal bands are observed experimentally instead of a single one. This may explain the absence of marked serrations on the experimental loading curve in contrast to the idealized simulation. No such propagative behavior is observed for the hexagon lattice of Fig. 30. In bending-dominated structures, plasticity initiates in all cells simultaneously and similarly in each cell, *i.e.* the strain field is almost periodic. In the simulation of Fig. 30 (left), strain localization phenomena are observed in some struts in tension. This explains the few stress drops in the red curve of Fig. 28. While sharp localization is obtained in the simulation based on an idealized geometry, the experiments reveal smoother responses due to the heterogeneous and imperfect nature of the samples.

6. Discussion

We characterized the development of material instabilities in architectured material depending on the geometrical features of the lattice, both numerically and experimentally. This study deals only with basic geometries which tessellate the plane in a periodic and regular manner. Graded microstructures should also be considered, combining bending- and stretch-dominated lattices with slowly varying evolution of the geometry in the sample. Another important issue is to understand the mechanisms that drive localization in the struts for stretch-dominated lattices and in the nodes for bending-dominated lattices in order to take advantage of very localized or diffused plasticity in lattices.

Computational homogenization using periodic boundary conditions has been shown to be an appropriate tool to investigate the development of instabilities in architectured materials. However, we have seen that the choice of the number of primitive cells in the unit cell raise several issues during the propagation of instabilities, and could lead to missing localization modes due to the constraining effect of periodic boundary conditions. There is a dependence of the number of predicted instability modes on the number of cells in the unit cell. As explained by Vigliotti et al. (2014) dealing with the buckling of lattices, increasing the volume element size, *i.e.* increasing the cell number, leads to an increase of possible buckled configurations. They also analyzed the effect of the unit cell size on the homogenized model. Similar effects are expected in the case of material instabilities like Piobert-Lüders banding. Al Kotob et al., (2020) proposed a systematic method for the analysis of elastoplastic instabilities. This method perturbs the periodic boundary conditions and makes it possible to compute elementary modes of localization. In Gong et al. (2005), the authors present a method based on Bloch waves developed by Triantafyllidis and co-workers to discuss the RVE size necessary to capture the buckling modes of a periodic column. Combescure et al., (2020), Combescure and Elliott, (2017) reported different equilibrium configurations of honeycombs subjected to bi-axial compression computed on different volume element sizes. Using Bloch wave theory, they report the identification of modes involving a higher number of cells in the VE. It is necessary to identify the minimal number of cells to capture the most relevant instability modes for the structural behavior. The previous methods were applied mainly to geometric instabilities. The case of material instabilities associated with the softening constitutive branch is different in nature, but the present work shows that the problem can be tackled by means of periodic nonlinear homogenization provided that a large enough number of primitive cells are considered.

Geers et al. (2010) addressed the main issues of multi-scale computational homogenization. They presented computational homogenization of emerging and evolving localization bands as an open issue to be tackled. First-order and second-order computational homogenization schemes present several limitations in the presence of localization. Localization causes ill-posedness of the boundary value problem on the representative RVE and questions the assumption of scale separation in continuous homogenization. Classical homogenization cannot be used beyond the onset of strain localization. Coenen et al. (2012) developed a computational homogenization-localization framework and overcame the violation of the separation of scale by enriching the macro-scale continuum with a displacement discontinuity. The case of static strain ageing instabilities is different in the sense that the softening branch is followed by subsequent hardening restoring the well–posedness of the boundary value problem. These issues were discussed in (Mazière and Forest, 2015; Rezaee Hajidehi and Stupkiewicz, 2017) where a regularization method based on gradient and micromorphic model enhancement was proposed to regularize the localization problem. The subsequent hardening is responsible for the band front propagation in contrast to continuing localization or damage in static bands. The issues about the size of the unit cell impact the mechanical behavior only during the phase of instabilities propagation. After this transition, the behavior for all number of unit cells is the same.

The experiments presented in this paper confirmed partially the predictions of the numerical models based on periodic homogenization on the one hand and on the full field simulation of the actual samples. In stretch-dominated lattices, the formation of Piobert-Lüders bands in some struts trigger the formation of a (or several) macroscopic band(s) that propagate through the whole sample. In bending-dominated lattices, no macroscopic propagative band emerges. According to the last snaps of Fig. 28 and Fig. 27(d) that represent the strain maps just before the failure of each specimen, additional conclusions can be drawn. For the 0°-oriented and the 45°-oriented square lattices, the macroscopic strains at fracture respectively are 0.067 and 0.112 whereas the maximum local strain values in the Y direction are 0.13 and 0.035. The non-propagating behavior of bending-dominated may be explained by the fact that the local strain level is not high enough to trigger the propagation of the Piobert–Lüders band in the struts. In Fig. 24(d), the band has a strain level of 0.05 during its propagation. In other terms, the structure fails before the Piobert-Lüders strain has been reached at the nodes of the lattice. On the one hand, stretch-dominated lattices experience higher plastic strain levels in the struts even at low macroscopic deformation, while, on the other hand, bending-dominated lattices undergo much larger macroscopic deformation without high levels of local plastic strain. Thus, one can choose bending-dominated structures for applications at large deformations or stretched-dominated structures if a stiff behavior is wanted.

Results are calling for improvements to enhance the precision in the tracking of propagation of material instabilities in lattices with higher number of cells and larger strut cross section. Moreover, side/edge effects in the form of free–standing struts in the square lattice for instance are significant in the experimental results. There is a competition between the size of the unit cell, large enough to be tracked with DIC and the number of cells in the specimen in order to neglect the edge effects. Next samples should integrate more cells. It is essential that boundary conditions should be well defined and side effects reduced to a minimum. The comparison between theory and experiments regarding the stretch-dominated behavior of the square lattice requires more precision. Theory predicts propagation in the lattice which is not observed clearly in the experiments. Simulations have been run with perturbed direction of the solicitation and show softened localisation in the cross sections of the numerical sample. This may confirm that perfect orientation of the sample is a necessary condition to observe relevant localisation and macroscopic behavior. The question of the sensibility to imperfections deserves a more detail study which is not the purpose of this work.

7. Concluding remarks

The uniaxial tensile response of 2D lattice with propagation of plastic instabilities known as Piobert-Lüders bands has been analyzed for 4 geometries: triangle, square at 0° and 45° and hexagonal lattices. We have demonstrated that the tensile response of each lattice depends on its either stretch- or bending-dominated behavior. It is then possible to control the initiation and the propagation of material instabilities through architectures.

For bending-dominated structures, the macroscopic strain–stress curve is characterized by 2 regimes: (i) initial linear elastic regime and (ii) plastic strain starting in the plastic hinges of the lattice. It does not exhibit any peak or plateau stress. Plasticity initiates at the same time, at all nodes and in the same manner. Then, it spreads still identically from the plastic hinges. A single cell RVE is needed to simulate this behavior. Those lattices do not propagate instabilities except for the orientation that align one strut with the loading direction. It is the case for the hexagon oriented at 0°. In this case, the aligned struts can be stretched. A plastic band propagates in each well-oriented strut of the lattice.

For stretch-dominated lattices, the macroscopic stress–strain curve is characterized by 3 regimes: (i) initial linear elastic regime, (ii) peak and plateau stress as a result of the initiation and propagation of Piobert-Lüders bands in the main stretched struts and (iii) post-propagation hardening behavior with increasing plastic strain. Between two neighboring cells, localization and propagation of plastic instabilities is different during the second regime. The behavior of plastic instabilities depends on the lattice geometry during its initiation and propagation. Once all cells are plastic (iii), the behavior becomes identical in the whole lattice. It is therefore necessary to have a volume element larger than a single primitive cell in order to observe the propagative behavior from cell to cell. The triangle cell enhances the possibility to control the level of stress for the propagation of plastic instability, *i.e.* the stress level of the plateau. This stretched-dominated lattice allows to tune this stress level thanks to the orientation of the lattice to the loading direction. The more struts can undergo plastic instability, the higher the stress plateau is.

Experimental testing on ARMCO® steel specimens architectured by laser cutting essentially confirmed the periodic homogenization predictions. In bending-dominated lattices plasticity develops at the nodes and no further propagation of bands was observed. In stretch-dominated lattices plasticity develops in the struts into propagating bands. Features of the band propagation, peak and stress, plateau in the structure could not be well identified on the stress–strain curves due to important side effects and experimental imperfections.

Finally, those remarks seem to confirm that a well-chosen lattice architecture and orientation can control the initiation and the propagation of Piobert-Lüders bands for a given mechanical load. The choice of the architectures can be made to meet a specific objective. The two different behaviors of plastic instabilities in bending-dominated or stretch-dominated and the possibility to combine those two in a single structure open the path to material instability-based architectured materials.

Declaration of Competing Interest

The authors declare that they have no known competing financial interests or personal relationships that could have appeared to influence the work reported in this paper.

Acknowledgments

This study was funded by Agence Nationale de la Recherche through the ANR ALMARIS project (Grant No. ANR-16-CE08-0001). The support of the Centre des Matériaux for conducting the experiments is gratefully acknowledged. Thanks are due in particular to Stéphanie Dang and Abdennour Meddour from Mines ParisTech.

References

Alonso, I.Q., Fleck, N., 2007. Damage tolerance of an elastic-brittle diamond-celled honeycomb. Scr. Mater. 56, 693–696. URL:http://www.sciencedirect.com/science/article/pii/S1359646207000152,https://doi.org/10.1016/j.scriptamat.2006.12.027..

Ashby, M., 2006. The properties of foams and lattices. Philos. Trans. R. Soc. A: Math., Phys. Eng. Sci. 364, 15–30. URL:https://royalsocietypublishing.org/doi/abs/10.1098/rsta.2005.1678,https://doi.org/10.1098/rsta.2005.1678..

Ashby, M., 2013. Designing architectured materials. Scr. Mater. 68, 4–7. URL:http://www.sciencedirect.com/science/article/pii/S1359646212002965,https://doi.org/10.1016/j.scriptamat.2012.04.033. architectured Materials..

Ashby, M., Bréchet, Y., 2003. Designing hybrid materials. Acta Mater. 51, 5801–5821. URL:http://www.sciencedirect.com/science/article/pii/S1359645403004415,https://doi.org/10.1016/S1359-6454(03)00441-5. the Golden Jubilee Issue. Selected topics in Materials Science and Engineering: Past, Present and Future..

Auffray, N., Dirrenberger, J., Rosi, G., 2015. A complete description of bi-dimensional anisotropic strain-gradient elasticity. Int. J. Solids Struct. 69–70, 195–206. URL: http://www.sciencedirect.com/science/article/pii/S0020768315002577, https://doi.org/10.1016/j.ijsolstr.2015.04.036..

Al Kotob, M., Combescure, C., Mazière, M., Rose, T., Forest, S., 2020. A general and efficient multistart algorithm for the detection of loss of ellipticity in elastoplastic structures. International Journal for Numerical Methods in Engineering 121 (5), 842–866. https://doi.org/10.1002/nme.6247.

Ballarin, V., Soler, M., Perlade, A., Lemoine, X., Forest, S., 2009. Mechanisms and modeling of bake-hardening steels: Part i. uniaxial tension. Metall. Mater. Trans. A 40, 1367–1374. https://doi.org/10.1007/s11661-009-9813-5.

Besson, J., Cailletaud, G., Forest, J.L.C.S., 2009. Mécanique non linéaire des matériaux. https://doi.org/10.1007/978-90-481-3356-7.

Bonfanti, A., Bhaskar, A., 2018. Elastoplastic response and recoil of honeycomb lattices. Eur. J. Mech. – A/Solids 71, 77–88. URL:http://www.sciencedirect.com/science/article/pii/S0997753817301122,https://doi.org/10.1016/j.euromechsol.2017.12.003..

Bonfanti, A., Bhaskar, A., Ashby, M., 2016. Plastic deformation of cellular materials, in: Reference Module in Materials Science and Materials Engineering. Elsevier. URL:http://www.sciencedirect.com/science/article/pii/B9780128035818030095,https://doi.org/10.1016/B978-0-12-803581-8.03009-5..

Bouaziz, O., Bréchet, Y., Embury, J., 2008. Heterogeneous and architectured materials: A possible strategy for design of structural materials. Adv. Eng. Mater. 10, 24–36. URL:https://onlinelibrary.wiley.com/doi/abs/10.1002/adem.200700289,https://doi.org/10.1002/adem.200700289..

Bréchet, Y., Embury, J., 2013. Architectured materials: Expanding materials space. Scr. Mater. 68, 1–3. URL:http://www.sciencedirect.com/science/article/pii/S135964621200499X,https://doi.org/10.1016/j.scriptamat.2012.07.038. architectured Materials..

Bréchet, Y.J.M., 2013. Chapter 1. architectured materials: An alternative to microstructure control for structural materials design? a possible playground for bio-inspiration?, in: Materials Design Inspired by Nature: Function Through Inner Architecture. The Royal Society of Chemistry, pp. 1–16.https://doi.org/10.1039/9781849737555-00001..

Côté, F., Deshpande, V., Fleck, N., Evans, A., 2006. The compressive and shear responses of corrugated and diamond lattice materials. Int. J. Solids Struct. 43, 6220–6242. URL:http://www.sciencedirect.com/science/article/pii/S0020768305004919,https://doi.org/10.1016/j.ijsolstr.2005.07.045..

Coenen, E., Kouznetsova, V., Geers, M., 2012. Multi-scale continuous–discontinuous framework for computational-homogenization-localization. J. Mech. Phys. Solids 60, 1486–1507. URL:http://www.sciencedirect.com/science/article/pii/S0022509612000749,https://doi.org/10.1016/j.jmps.2012.04.002..

Combescure, C., Elliott, R., 2017. Hierarchical honeycomb material design and optimization: Beyond linearized behavior. Int. J. Solids Struct. 115. https://doi.org/10.1016/j.ijsolstr.2017.03.011.

Combescure, C, Elliott, RS, Triantafyllidis, N, 2020. Deformation Patterns and their Stability in Finitely Strained Circular Cell Honeycombs. Journal of the Mechanics and Physics of Solids. https://doi.org/10.1016/j.jmps.2020.103976 103976.

dell'Isola, F., Seppecher, P., Alibert, J.J., Lekszycki, T., Grygoruk, R., Pawlikowski, M., Steigmann, D., Giorgio, I., Andreaus, U., Turco, E., Gołaszewski, M., Rizzi, N., Boutin, C., Eremeyev, V.A., Misra, A., Placidi, L., Barchiesi, E., Greco, L., Cuomo, M., Cazzani, A., Corte, A.D., Battista, A., Scerrato, D., Eremeeva, I.Z., Rahali, Y., Ganghoffer, J.F., Müller, W., Ganzosch, G., Spagnuolo, M., Pfaff, A., Barcz, K., Hoschke, K., Neggers, J., Hild, F., 2018. Pantographic metamaterials: an example of mathematically driven design and of its technological challenges. Continuum Mech. Thermodyn. https://doi.org/10.1007/s00161-018-0689-8.

Deshpande, V., Ashby, M., Fleck, N., 2001. Foam topology: bending versus stretching dominated architectures. Acta Mater. 49, 1035–1040. URL:http://www.sciencedirect.com/science/article/pii/S1359645400003797,https://doi.org/10.1016/S1359-6454(00)00379-7..

Dogui, A., Sidoroff, F., 1986. Rhéologie anisotrope en grandes déformations, rhéologie des matériaux anisotropes. Ed. C. Huet, D. Bourguoin, S. RIchemond, Cepadues Toulouse, 69–78..

Fleck, N.A., Qiu, X., 2007. The damage tolerance of elastic–brittle, two-dimensional isotropic lattices. J. Mech. Phys. Solids 55, 562–588. URL:http://www.sciencedirect.com/science/article/pii/S0022509606001359,https://doi.org/10.1016/j.jmps.2006.08.004..

Geers, M., Kouznetsova, V., Brekelmans, W., 2010. Multi-scale computational homogenization: Trends and challenges. J. Computat. Appl. Math. 234, 2175–2182. URL:http://www.sciencedirect.com/science/article/pii/S0377042709005536,https://doi.org/10.1016/j.cam.2009.08.077. fourth International Conference on Advanced COmputational Methods in ENgineering (ACOMEN..

Gibson, J., Ashby, M., 1999. Cellular Solids: Structures and Properties. Cambridge University Press.

Gong, L., Kyriakides, S., Triantafyllidis, N., 2005. On the stability of kelvin cell foams under compressive loads. J. Mech. Phys. Solids 53, 771–794. URL: http://www.sciencedirect.com/science/article/pii/S0022509604001899,https://doi.org/10.1016/j.jmps.2004.10.007..

Guoming, H., Hui, W., Youlin, Z., Wujun, B., 2006. A large deformation model for the elastic moduli of two-dimensional cellular materials. J. Wuhan Univ. Technol.-Mater. Sci. Ed. 21, 154.

Hallai, J.F., Kyriakides, S., 2011. On the effect of lüders bands on the bending of steel tubes. part i: Experiments. Int. J. Solids Struct. 48, 3275–3284. URL:http://www.sciencedirect.com/science/article/pii/S0020768311002472,https://doi.org/10.1016/j.ijsolstr.2011.06.024..

He, Y., Zhou, Y., Liu, Z., Liew, K., 2018. Buckling and pattern transformation of modified periodic lattice structures. Extreme Mech. Lett. 22, 112–121. URL: http://www.sciencedirect.com/science/article/pii/S2352431618300841, https://doi.org/10.1016/j.eml.2018.05.011..

Kyriakides, S., Ok, A., Corona, E., 2008. Localization and propagation of curvature under pure bending in steel tubes with lüders bands. Int. J. Solids Struct. 45, 3074–3087. URL: http://www.sciencedirect.com/science/article/pii/S0020768308000255,https://doi.org/10.1016/j.ijsolstr.2008.01.013..

Ladevèze, P., 1980. Sur la théorie de la plasticité en grandes déformations. ENS-Cachan-LMT Internal Report.

Latture, R.M., Begley, M.R., Zok, F.W., 2018. Design and mechanical properties of elastically isotropic trusses. J. Mater. Res. 33, 249–263. https://doi.org/10.1557/jmr.2018.2.

Lüders, W., 1860. Über die äusserung der elasticität an stahlartigen eisenstäben und stahlstäben, und über eine beim biegen solcher stäbe beobachtete molecularbewegung. Dinglers Polytech J5, 18–22.

Marais, A., Mazière, M., Forest, S., Parrot, A., Delliou, P.L., 2012. Identification of a strain-aging model accounting for lüders behavior in a c-mn steel. Phil. Mag. 92, 3589–3617. https://doi.org/10.1080/14786435.2012.699687.

Mazière, M., Forest, S., 2015. Strain gradient plasticity modeling and finite element simulation of lüders band formation and propagation. Continuum Mech. Thermodyn. 27, 83–104. https://doi.org/10.1007/s00161-013-0331-8.

Mazière, M., Luis, C., Marais, A., Forest, S., Gasperini, M., 2017. Experimental and numerical analysis of the lüders phenomenon in simple shear. Int. J. Solids Struct. 106–107, 305–314. URL:http://www.sciencedirect.com/science/article/pii/S0020768316301871,https://doi.org/10.1016/j.ijsolstr.2016.07.026..

Nassar, H., He, Q.C., Auffray, N., 2016. A generalized theory of elastodynamic homogenization for periodic media. Int. J. Solids Struct. 84, 139–146. URL: http://www.sciencedirect.com/science/article/pii/S0020768316000445, https://doi.org/10.1016/j.ijsolstr.2016.01.022..

Niknam, H., Akbarzadeh, A., 2018. In-plane and out-of-plane buckling of architected cellular plates: numerical and experimental study. Compos. Struct. 206, 739–749. URL:http://www.sciencedirect.com/science/article/pii/S0263822318321809, https://doi.org/10.1016/j.compstruct.2018.08.026..

Onal, E., Frith, J.E., Jurg, M., Wu, X., Molotnikov, A., 2018. Mechanical properties and in vitro behavior of additively manufactured and functionally graded ti6al4v porous scaffolds. Metals 8. URL:https://www.mdpi.com/2075-4701/8/4/200, https://doi.org/10.3390/met8040200..

Piobert, G., 1842. Expérience sur la pénétration des projectiles dans le fer forgé. Mémoire de l'Artillerie 505..

Poncelet, M., Somera, A., Morel, C., Jailin, C., Auffray, N., 2018. An experimental evidence of the failure of cauchy elasticity for the overall modeling of a non-centro-symmetric lattice under static loading. Int. J. Solids Struct.147, 223–237. URL:http://www.sciencedirect.com/science/article/pii/S0020768318302221, https://doi.org/10.1016/j.ijsolstr.2018.05.028..

Rezaee Hajidehi, M., Stupkiewicz, S., 2017. Gradient-enhanced model and its micromorphic regularization for simulation of l++ders-like bands in shape memory alloys. Int. J. Solids Struct. https://doi.org/10.1016/j.ijsolstr.2017.11.021.

Rosi, G., Auffray, N., 2019. Continuum modelling of frequency dependent acoustic beam focussing and steering in hexagonal lattices. Eur. J. Mech. – A/Solids 77, 103803. URL:http://www.sciencedirect.com/science/article/pii/S0997753818309859,https://doi.org/10.1016/j.euromechsol.2019.103803..

Rosi, G., Placidi, L., Auffray, N., 2018. On the validity range of strain-gradient elasticity: a mixed static-dynamic identification procedure. Eur. J. Mech. – A/Solids 69, 179–191. URL: http://www.sciencedirect.com/science/article/pii/S0997753817305880,https://doi.org/10.1016/j.euromechsol.2017.12.005..

Schraad, M.W., Triantafyllidis, N., 1997. Scale effects in media with periodic and nearly periodic microstructures, Part I: macroscopic properties. J. Appl. Mech. 64, 751–762.https://doi.org/10.1115/1.2788979, arXiv:https://asmedigitalcollection.asme.org/appliedmechanics/article-pdf/64/4/751/4726981/751_1.pdf..

Tankasala, H., Deshpande, V., Fleck, N., 2017. Tensile response of elastoplastic lattices at finite strain. J. Mech. Phys. Solids 109, 307–330. URL: http://www.sciencedirect.com/science/article/pii/S0022509616307967,https://doi.org/10.1016/j.jmps.2017.02.002..

Triantafyllidis, N., Bardenhagen, S., 1996. The influence of scale size on the stability of periodic solids and the role of associated higher order gradient continuum models. J. Mech. Phys. Solids 44, 1891–1928. URL: http://www.sciencedirect.com/science/article/pii/0022509696000476,https://doi.org/10.1016/0022-5096(96)00047-6..

Tsukahara, H., Iung, T., 1998. Finite element simulation of the piobert–lüders behavior in an uniaxial tensile test. Mater. Sci. Eng.: A 248, 304–308. URL: http://www.sciencedirect.com/science/article/pii/S0921509397008575, https://doi.org/10.1016/S0921-5093(97)00857-5..

Turco, E., Misra, A., Pawlikowski, M., dell'Isola, F., Hild, F., 2018. Enhanced piola–hencky discrete models for pantographic sheets with pivots without deformation energy: numerics and experiments. Int. J. Solids Struct. 147, 94–109. URL: http://www.sciencedirect.com/science/article/pii/S0020768318302002,https://doi.org/10.1016/j.ijsolstr.2018.05.015..

Vigliotti, A., Deshpande, V.S., Pasini, D., 2014. Non linear constitutive models for lattice materials. J. Mech. Phys. Solids 64, 44–60. URL: http://www.sciencedirect.com/science/article/pii/S0022509613002238,https://doi.org/10.1016/j.jmps.2013.10.015..

Wang, A.J., McDowell, D., 2004. In-plane stiffness and yield strength of periodic metal honeycombs. J. Eng. Mater. Technol. 126, 137–156.

Wang, A.J., McDowell, D., 2005. Yield surfaces of various periodic metal honeycombs at intermediate relative density. Int. J. Plasticity 21, 285–320. URL: http://www.sciencedirect.com/science/article/pii/S0749641904000026, https://doi.org/10.1016/j.ijplas.2003.12.002..

Zok, F.W., Latture, R.M., Begley, M.R., 2016. Periodic truss structures. J. Mech. Phys. Solids 96, 184–203. URL: http://www.sciencedirect.com/science/article/pii/S0022509615300983,https://doi.org/10.1016/j.jmps.2016.07.007..